

Programming a quantum computer with quantum instructions

M. Kjaergaard^{†,1,*} M. E. Schwartz,^{2,†} A. Greene,¹ G. O. Samach,^{1,2} A. Bengtsson,^{1,3} M. O’Keeffe,² C. M. McNally,¹ J. Braumüller,¹ D. K. Kim,² P. Krantz,^{1,‡} M. Marvian,^{1,4} A. Melville,² B. M. Niedzielski,² Y. Sung,¹ R. Winik,¹ J. Yoder,² D. Rosenberg,² K. Obenland,² S. Lloyd,^{1,4} T. P. Orlando,¹ I. Marvian,⁵ S. Gustavsson,¹ and W. D. Oliver^{1,2,6,7}

¹Research Laboratory of Electronics, Massachusetts Institute of Technology, Cambridge, MA, USA

²MIT Lincoln Laboratory, Lexington, MA, USA

³Microtechnology and Nanoscience, Chalmers University of Technology, Göteborg, Sweden

⁴Department of Mechanical Engineering, Massachusetts Institute of Technology, Cambridge, MA, USA

⁵Departments of Physics & Electrical and Computer Engineering, Duke University, Durham, NC, USA

⁶Department of Physics, Massachusetts Institute of Technology, Cambridge, MA, USA

⁷Department of Electrical Engineering & Computer Science, Massachusetts Institute of Technology, Cambridge, MA, USA

(Dated: December 29, 2020)

The equivalence between the instructions used to define programs and the input data on which the instructions operate is a basic principle of classical computer architectures and programming [1]. Replacing classical data with quantum states enables fundamentally new computational capabilities with scaling advantages for many applications [2, 3], and numerous models have been proposed for realizing quantum computation [4–6]. However, within each of these models, the quantum data are transformed by a set of gates that are compiled using solely classical information. Conventional quantum computing models thus break the instruction-data symmetry: classical instructions and quantum data are not directly interchangeable. In this work, we use a density matrix exponentiation protocol [7] to execute quantum instructions on quantum data. In this approach, a fixed sequence of classically-defined gates performs an operation that uniquely depends on an auxiliary quantum instruction state. Our demonstration relies on a 99.7% fidelity controlled-phase gate implemented using two tunable superconducting transmon qubits, which enables an algorithmic fidelity surpassing 90% at circuit depths exceeding 70. The utilization of quantum instructions obviates the need for costly tomographic state reconstruction and recompilation, thereby enabling exponential speedup for a broad range of algorithms, including quantum principal component analysis [7], the measurement of entanglement spectra [8], and universal quantum emulation [9].

In classical programmable computers, instructions are specified in the same medium as the data they process (Figure 1a), such that programs can be treated interchangeably with data. This property, known as homoiconicity [10], is a hardware-level property of all classical computers based on the von Neumann architecture [11] as well as of higher-level programming languages like Lisp, Julia, and Wolfram.

In all previous experimentally-realized quantum computational systems (e.g., Refs. [12–14]), the relation between instructions and data is fundamentally different. Quantum programs generally comprise a classically-defined list of gates (the instructions) that are applied to a quantum processor (the data) using intermediary control hardware (Figure 1b). Thus, this programming architecture is non-homoiconic: the instructions are manifestly classical, whereas the data are quantum mechanical. Furthermore, if an algorithm requires instructions derived from the present quantum state of the processor, that information must first be extracted from the quantum system (incurring exponential overhead [15]), classically processed and compiled, and then appended to the

classical instruction list [16–22]. Such a costly reconstruction process would create significant bottlenecks in quantum algorithms at scale [23, 24].

Here, we demonstrate the use of quantum instructions to implement a quantum program – a unitary operation whose parameters are given by the properties of a quantum state [25–27] – on a superconducting quantum processor. Our approach is based on density matrix exponentiation (DME), a protocol originally introduced in the context of quantum machine learning [7]. DME is executed by a series of repeated classical control pulses (Fig. 1c), which, in contrast to conventional quantum programs (Fig. 1b), carry no information about the instruction set. Rather, the instructions are encoded in the “instruction qubits” (density matrix ρ), which determine the unitary operations performed on the “data qubits” (density matrix σ). Thus, both instructions and data are stored in quantum states [25], and together they constitute a quantum computing analogue of homoiconicity. We apply DME to a system comprising two superconducting qubits: a data qubit prepared in state σ , and an instruction qubit prepared in state ρ . In this case, DME implements a unitary rotation on the data qubit about an axis parallel to instruction state. At this scale, the quantum instruction state and its resulting unitary operation are easily predicted and straightforward to reconstruct. However, extending the number of instruction qubits to the supremacy regime [12], in which a classically-specified

* mortenk@mit.edu

† Authors contributed equally to this work

‡ Current address: Microtechnology and Nanoscience, Chalmers University of Technology

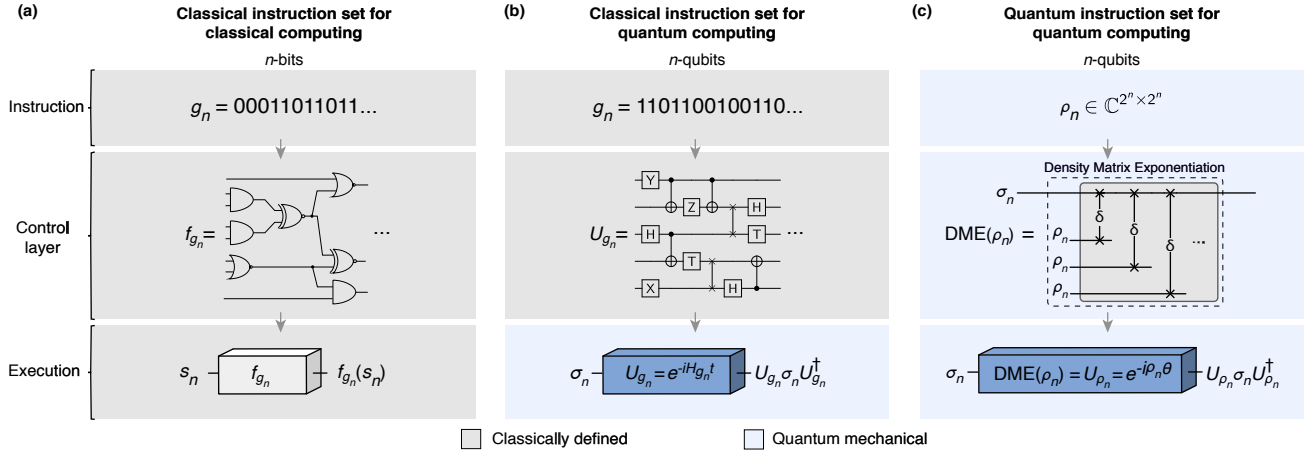


FIG. 1. **Schematic representations of computing architectures.** **a**, Classical instruction set for classical computing. Instructions are defined by a classical bit string g_n that uniquely determines a boolean-logic function f_{g_n} comprising single-bit and two-bit gates. The control layer executes the resulting circuit on data bits s_n to produce the output $f_{g_n}(s_n)$. **b**, Classical instruction set for conventional quantum computing. The instruction set encoding a quantum circuit is generated using classical resources. Instructions are defined by a classical bit string g_n that uniquely determines a unitary operation U_{g_n} comprising single-qubit and two-qubit gates. The control layer uses solely classical hardware to generate the gate sequence and applies it to the quantum hardware (data qubits σ_n) to execute the unitary evolution $U = \exp(-iH_{g_n}t)$, where H_{g_n} is the quantum circuit Hamiltonian, to produce the output $U_{g_n}\sigma_n U_{g_n}^\dagger$. **c**, Quantum instruction set for quantum computing using the density matrix exponentiation (DME) algorithm. The instruction set encoding a quantum circuit is stored in the instruction qubits ρ_n . The control layer uses classical hardware to generate N partial SWAP operations (see text) over a small, classically chosen rotation angle $\delta = \theta/N$, where θ is an algorithm-dependent angle. These classically defined operations (grey region) contain no information about the operation implemented on the data qubits (σ_n). Using a Trotterization approach (see text), the partial SWAP operations are repeatedly applied to the quantum hardware (blue region) – data qubits σ_n and identically prepared copies of the instruction qubits ρ_n – to execute the unitary operation $U = \exp(-i\rho_n\theta) \equiv \exp(-iH_{g_n}t)$, for appropriately chosen g_n . The output $U_{\rho_n}\sigma_n U_{\rho_n}^\dagger$ is equivalent to $U_{g_n}\sigma_n U_{g_n}^\dagger$ to within an error $\mathcal{O}(\theta^2/N)$ for appropriately chosen ρ_n (see text).

sequence of gates can produce a quantum state that is too complex to predict and too large to tomographically reconstruct, leads to a remarkable programming and operational framework: while it would be completely impractical to ascertain the quantum instructions stored in an unknown state ρ , one can nonetheless use these instructions to execute a quantum program (as defined above). Programs based on quantum instructions implemented with DME enable a class of efficient algorithms addressing both quantum computation (using ρ to manipulate σ) and quantum metrology (using σ to study ρ). The afforded quantum advantage generally stems from the fact that DME directly implements unitary operations $e^{-i\rho\theta}$ at the quantum hardware layer, obviating the need for tomographic reconstruction of the instruction state ρ on which these applications are based [7, 15, 28]. One example is private quantum software execution, whereby the action of an unknown (private) unitary U on an arbitrary quantum state may be efficiently emulated using a relatively small set of known input-output relations $\{\rho_{\text{in}}\} \xrightarrow{U} \{\rho_{\text{out}}\}$ [9], far fewer than would be required to compromise the security of U via its tomographic reconstruction. Quantum instructions also enable quantum advantage for quantum semi-definite programming [29] and sample-optimal Hamiltonian simulation [28]. In addition, quantum phase estimation executed using DME can extract with error ϵ the dominant eigenvalues and eigenvectors of ρ – principal component analysis – using only $\mathcal{O}(\theta^2/\epsilon)$ copies

of ρ [7, 28]. Even when ρ is a large entangled state, DME can efficiently reveal its entanglement spectrum, a form of reduced-complexity benchmarking [8].

The DME protocol

Conceptually, DME implements the unitary operation $U = e^{-i\rho\theta}$ on the data qubit(s) according to the instruction state ρ and an algorithm-dependent angle θ . If the data and instruction states are single-qubit pure states σ and ρ , DME rotates σ by an angle θ about an axis defined by the Bloch vector of ρ . More generally, σ and ρ are multi-qubit states, and they need not be pure states. The protocol that implements DME partitions U into a sequence of N steps (Fig. 2a), each comprising a “partial SWAP” operation $\delta\text{SWAP} \equiv e^{-i\text{SWAP}\delta}$ [30] that is applied to σ and ρ [7]. The protocol relies on the relation:

$$\begin{aligned} \text{Tr}_\rho [e^{-i\text{SWAP}\delta}\sigma \otimes \rho e^{i\text{SWAP}\delta}] &= \sigma - i\delta[\rho, \sigma] + \mathcal{O}(\delta^2) \\ &= e^{-i\rho\delta}\sigma e^{i\rho\delta} + \mathcal{O}(\delta^2). \end{aligned} \quad (1)$$

That is, σ undergoes unitary evolution of the form $e^{-i\rho\delta}$ (to first order in δ , see Supplementary Methods), rotating by a small angle $\delta = \theta/N$. By the reciprocity of SWAP operations, ρ undergoes a complementary unitary evolution about σ , leaving it in a state that differs from the original quantum instruction. As a result, the instruction qubits must be refreshed at each step to provide a new, identical copy of the instruction state ρ . Repeating these steps N times (Fig. 2a)

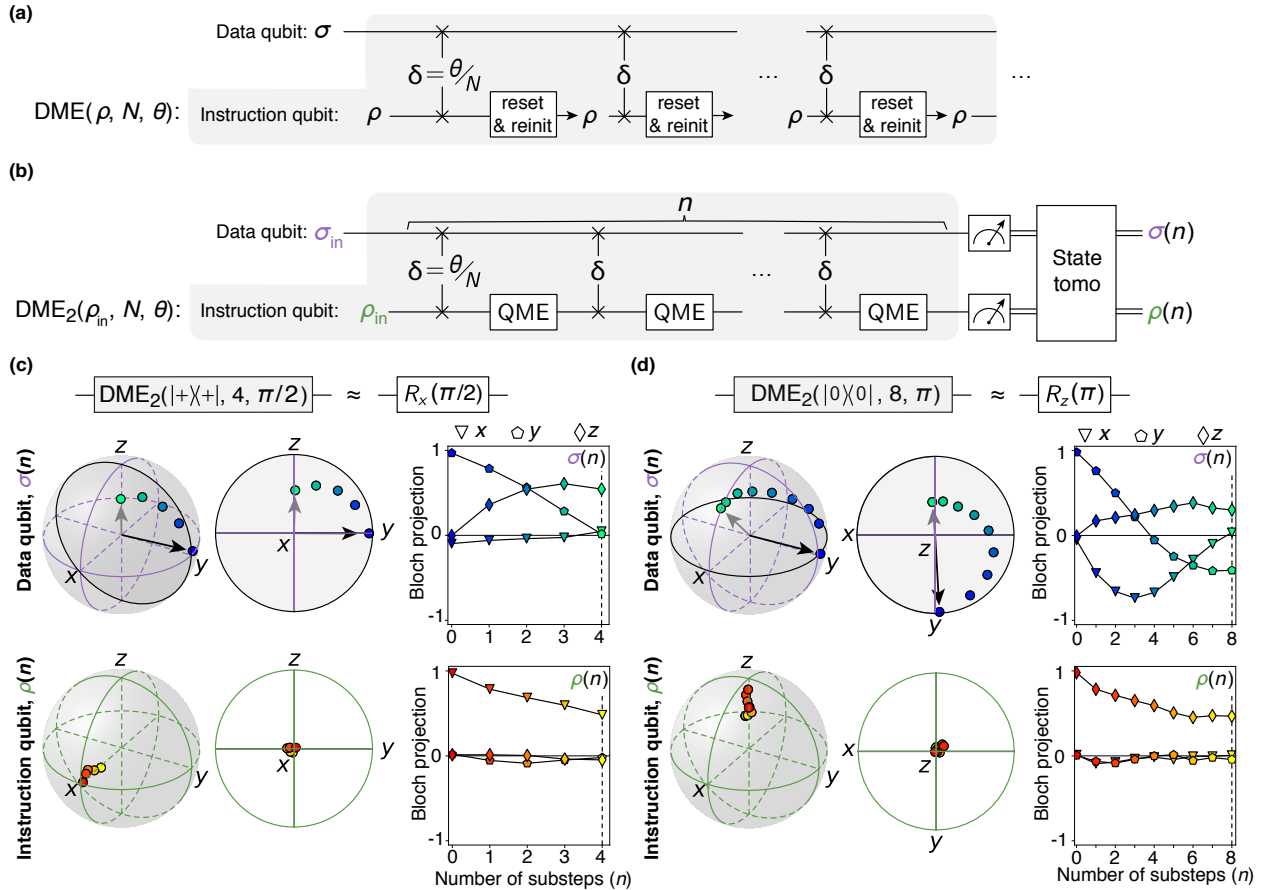


FIG. 2. **Demonstration of quantum instructions.** **a** Density Matrix Exponentiation (DME) algorithm using active reset and reinitialization to reprepare the instruction state ρ after each δ SWAP operation. **b** Implementation of DME_2 , in which quantum measurement emulation (QME) is used to approximately reinitialize the instruction qubit to ρ_{in} without active reset and repreparation (see text for details). The substep parameter n is stepped from 0 to N . In the experiment, we perform n rounds of δ SWAP + QME, measure the two-qubit density matrix, and trace over each subsystem to extract the individual data and instruction qubit density matrices ($\sigma(n)$ and $\rho(n)$ respectively). **c** Substeps of $DME_2(|+\rangle|+, 4, \pi/2)$, corresponding to $R_x(\pi/2)$ on the target qubit at the final step ($n = N$). Black lines are guides to the eye. **d** Substeps of $DME_2(|0\rangle|0\rangle, 8, \pi)$, corresponding to $R_z(\pi)$ on the target qubit at $n = N$.

approximately yields the desired operator,

$$DME(\rho, N, \theta) \rightarrow e^{-i\rho\theta} + \mathcal{O}\left(\frac{\theta^2}{N}\right), \quad (2)$$

a result that is closely related to the Trotterization of non-commuting Hamiltonians to perform quantum simulations [31]. Similar to dividing a quantum simulation into smaller steps to reduce errors stemming from the Trotter approximation, partitioning DME into more steps (increasing N), with a smaller partial SWAP angle δ per step, reduces the DME discretization error. The trade-off for increased precision is a need for more copies of the quantum instructions. There are three general approaches to supplying the N copies of the instruction state ρ needed to execute DME:

1. Teleport copies of the quantum instructions from a third party to the qubits comprising ρ .
2. Identically prepare the instructions on N copies of ρ

(hardware parallelization, Figure 1c);

3. Identically prepare the same set of qubits comprising ρ after each δ SWAP (sequential preparation in time, Figure 2a).

In this work, we choose option 3: we refresh the same instruction qubit to avoid the need for teleportation or large numbers of instruction qubits, and to allow us to easily vary N .

A new approach to generating N copies of ρ

The most obvious approach for using one qubit to generate N copies of ρ (Figure 2a) is to use measurement-conditioned active feedback to reset the instruction qubit to its ground state and then re-prepare the instruction state ρ [32]. However, due to measurement infidelity and the decoherence that occurs during the relatively long duration of the requisite measurement, feedback, and preparation steps,

the conventional active-reset approach would introduce an unacceptable level of errors on current quantum processors. Here, to minimize such errors and achieve the largest possible circuit depths with our qubits, we instead introduce an alternative approach (Figure 2b) called quantum measurement emulation (QME), that approximately reinitializes the instruction qubit in the time required for a single qubit gate.

QME is a probabilistic operation that mimics an ensemble averaged qubit measurement. For intuition, note that for a sufficiently small angle δ , the states of the two qubits are only slightly altered after a δ SWAP operation. In this case, a projective measurement of the instruction qubit in the eigenbasis of ρ would reset the instruction qubit to its original state with high probability. Similarly, an unconditioned ensemble averaged measurement of many such identically prepared states (i.e. a measure-and-forget approach) would reproduce the original ρ with only a slight depolarization. QME mimics this well-known result without actually performing a measurement by imposing a dephasing channel corresponding to the axis of ρ .

The QME operation (Figure 2b) randomly applies either an identity gate ($\mathbb{1}$) or a π -rotation in the instruction qubit eigenbasis, according to a Bernoulli process with probability $p = 0.5$:

$$\boxed{\text{QME}_\nu} = \begin{cases} \mathbb{1} & \text{with } p = 0.5 \\ R_\nu(\pi) & \text{with } 1 - p = 0.5 \end{cases} \quad (3)$$

where ν is a normalized vector parallel to the original instruction state. For instruction states aligned with the axes of the Bloch sphere, QME represents a probabilistic application of a Pauli gate. We incorporate QME into our circuit by interleaving δ SWAP and QME operations (Figure 2b). The QME operations are randomized within each instantiation of the circuit, and in the same spirit as randomized compiling [33], the outcomes of multiple such randomized instantiations are averaged to mimic a single circuit with an active reset of ρ .

The QME-enabled reset of ρ is approximate due to depolarization, which introduces an additional error term to the DME protocol. For our two-qubit demonstration with QME, denoted DME_2 , the unitary operation is (see Methods):

$$\text{DME}_2(\rho, N, \theta) \rightarrow e^{-i\rho\theta} + \underbrace{\mathcal{O}\left(\frac{\theta^2}{N}\right)}_{\text{discretization}} + \underbrace{\mathcal{O}\left(\frac{\theta^2}{N}\right)}_{\text{QME}}. \quad (4)$$

Despite the added error term, QME effectively supplies the requisite copies of ρ with less error than would be incurred with an active feedback approach in our system. Furthermore, its use here is not fundamental to our demonstration. An implementation of arbitrary, unknown quantum instructions could be performed using states from large quantum processors or by state-teleportation, and the underlying physics would be the same as those in this proof-of-principle experiment.

Implementing the DME_2 algorithm

We implement DME_2 using two frequency-tunable superconducting ‘asymmetric’ transmon qubits [34, 35] in an ‘xmon’ layout [36], operating with single-qubit gate fidelities exceeding 99.9% and a two-qubit controlled phase gate [37, 38] with 99.7% fidelity (see Methods). In Figures 2c and 2d, we interrupt the algorithm after $n \leq N$ steps and perform state tomography (see Methods) to visualize the evolution of the data-qubit and instruction-qubit. We use an initial state $\sigma_{\text{in}} = |+i\rangle\langle+i|$ for the data qubit, and we introduce the notation $\text{DME}_2(\rho_{\text{in}}, N, \theta)$ to indicate the initial instruction state ρ_{in} , total number of steps N , and the phase rotation θ . Figure 2c shows an implementation of $\text{DME}_2(|+\rangle\langle+|, 4, \pi/2)$. Since ρ is x -polarized, this instruction encodes the operation $R_X(\pi/2)$, a $\pi/2$ rotation about the x axis. Figure 2d shows an implementation of $\text{DME}_2(|0\rangle\langle 0|, 8, \pi)$, encoding the instruction $R_Z(\pi)$, a π rotation about the z axis. In both cases, σ undergoes a rotation about an axis defined by ρ_{in} , which is visible in the step-by-step tomographic reconstruction of the data qubit state $\sigma(n)$. QME maintains the polarization direction of the instruction qubit state $\rho(n)$, albeit with gradual depolarization consistent with the effects of the simulated measurement. The classically-defined δ SWAP operations are identical in these two cases; it’s the change in the instruction state ρ_{in} that causes a different operation on the data qubit. Thus, the implemented quantum program (here, a single-qubit operation) is uniquely determined by the state of another quantum system, a demonstration of quantum instructions.

We next assess DME_2 in the context of an imperfect quantum processor with noise-induced errors in addition to discretization (finite N) errors (Figure 3). Here, we fix target state $\sigma_{\text{in}} = |0\rangle\langle 0|$ and instruction state $\rho_{\text{in}} = |+i\rangle\langle+i|$, and vary total steps N . This allows us to probe the interplay between discretization error (which decreases with N) and noise-induced errors (which increases with N). We use two angles, $\theta = \pi$ and $\theta = \pi/2$, to elucidate the effects of changing the overall angle. For each experiment, we perform the full algorithm $\text{DME}_2(\rho_{\text{in}}, N, \theta)$ with many QME randomizations, tomographically reconstruct the final density matrix $\sigma(N)$, and calculate its fidelity to an ideal rotation with no discretization or processor error, as given by $\sigma_{\text{ideal}} = e^{-i\rho_{\text{in}}\theta}\sigma_{\text{in}}e^{i\rho_{\text{in}}\theta}$. σ_{ideal} can equivalently be thought of as a perfect unitary rotation, or as DME when implemented on an error-free processor with an infinite number of copies of the quantum instructions.

There are two sources of error we must consider in understanding the output of the DME_2 protocol: the approximate nature of the algorithm and imperfections in the quantum processor. To understand the discretization error, we calculate σ_{DME_2} , the outcome of a simulation of the DME_2 circuit (including discretization error) with perfect gates. We sample every possible combination of QME gates for a DME_2 circuit of length N and simulate the application of each circuit to the experimentally-measured $\rho_{\text{in}} \otimes \sigma_{\text{in}}$ (thus accounting

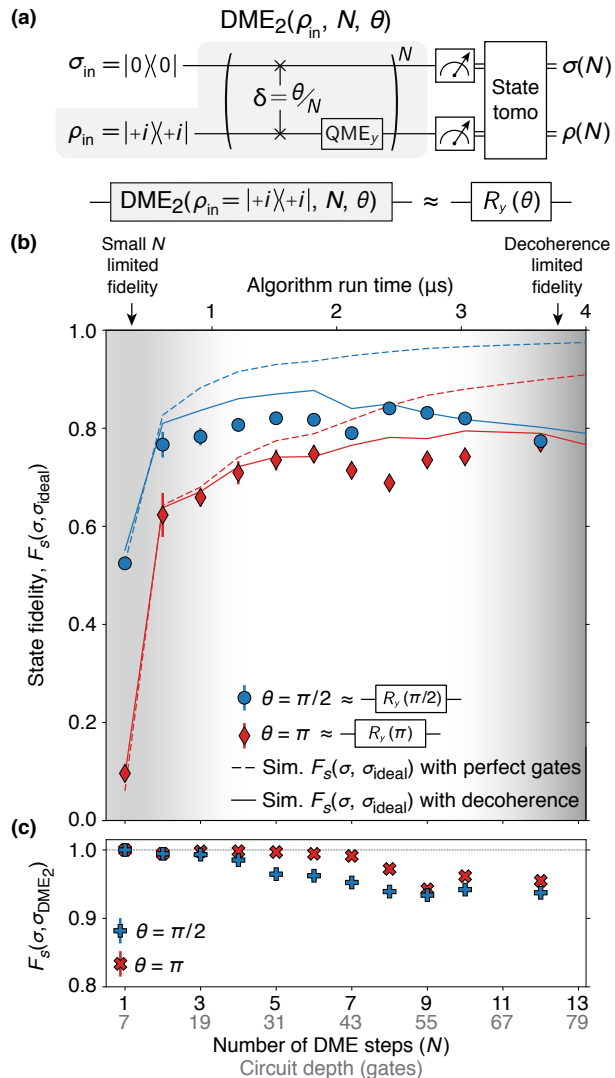


FIG. 3. **Algorithm performance as a function of N .** **a** Circuit schematic for $DME_2(|+i\rangle\langle +i|, N, \theta)$. Data qubit is initialized in $\sigma_{in} = |0\rangle\langle 0|$. **b** State fidelity (F_s) of the data qubit state σ to the ideal state $\sigma_{ideal} = e^{-i\rho_{in}\theta}\sigma_{in}e^{i\rho_{in}\theta}$ as a function of total DME steps (N). The instruction qubit is initialized to the $|+i\rangle\langle +i|$ -state, resulting in an ideal operation $e^{-i\rho_{in}\theta} = R_y(\theta)$. The x -axis shows the number of δ SWAP + QME steps N (bottom, black), circuit depth (bottom, gray), and active circuit clock time (top). Data for $\theta = \pi$ ($\pi/2$) are shown with red/ \diamond (blue/ \circ) markers. Dashed lines is the state fidelity between σ_{ideal} and a simulated output of the $DME_2(|+i\rangle\langle +i|, N, \theta)$ circuit, assuming perfect gates. The increasing fidelity with increasing N is a reflection of a reduction of the ‘discretization error’ scaling as $\mathcal{O}(\theta^2/N)$. Solid lines are the same simulation as shown in dashed lines, but with amplitude damping and depolarizing channels included in the circuit to model the effect of decoherence. **c** State fidelity of σ to a simulated output of the $DME_2(|+i\rangle\langle +i|, N, \theta)$ circuit with perfect gates (denoted $\sigma_{DME_2}(N)$). Error bars are determined from bootstrap analysis (see Methods).

for state-preparation errors). The fidelity $F_s(\sigma_{DME_2}, \sigma_{ideal})$ quantifies the error due solely to the approximate nature of DME_2 (Figure 3b, dashed lines). Figure 3c shows the fidelity of the measured state $\sigma(N)$ to the ideal algorithm

performance, $F_s(\sigma, \sigma_{DME_2})$. To circuit depth 73, this fidelity exceeds 0.90.

We next account for the effects of imperfections in the physical processor by building a model of DME_2 performance in the presence of processor noise. To the DME_2 circuit with perfect gates we add amplitude-damping and dephasing channels with coherence parameters consistent with independent measurements (see Methods). The fidelity between the model including decoherence effects and σ_{ideal} is plotted in Figure 3b (solid lines), and shows good agreement with experimental data, indicating we are mostly limited by decoherence effects, and not coherent errors in the gates.

Both the simulated and experimental curves reveal an interplay between finite N error and processor error. At small N , the error is dominated by the approximate nature of DME_2 as given in Eq. (4). The error is greater for larger θ , consistent with error scaling as $\mathcal{O}(\theta^2/N)$. For large N , the discretization error improves and the processor’s performance is instead limited by finite gate fidelity; here, the curves for $\theta = \pi$ and $\theta = \pi/2$ begin to converge. The algorithm is at its most accurate for intermediate N , where discretization error is relatively low and the circuit is sufficiently free of compounding physical errors. This tradeoff (improved performance with increasing circuit depth, until gate fidelities become limiting) is a generic property of Trotterized quantum algorithms on noisy processors in the absence of error-correction protocols [39].

To assess the error-budget of the quantum instruction execution independent of its operation on the target quantum state, we perform quantum process tomography. We experimentally reconstruct the process map of the channel implemented by DME_2 (denoted $\chi(\rho_{in}, N, \theta)$) for a set of instruction states given by the cardinal points on the Bloch sphere. For each ρ_{in} , we sweep N to find the optimal point N_{opt} , defined as that which has the highest process fidelity (see Methods) to the pure rotation $U_{ideal} = e^{-i\rho_{in}\theta}$. The mean N_{opt} for $\theta = \pi/2$ is 4, at circuit depth 25; for $\theta = \pi$ this increases to 8, at circuit depth 49.

In Figure 4 we plot the process fidelity at N_{opt} to several theoretical processes to elucidate the error budget in DME_2 . The fidelity to χ_{ideal} , corresponding to the perfect rotation U_{ideal} , is plotted in grey. $F_p(\chi, \chi_{ideal})$ is greater for $\theta = \pi/2$ than for $\theta = \pi$, as expected from the $\mathcal{O}(\theta^2/N)$ scaling of the discretization error, and is consistent for all cardinal settings of the instruction state. This process fidelity reflects the combination of errors arising from the Trotterized nature of density matrix exponentiation and the errors from imperfect gates and the approximate nature of QME.

We next compare our QME-enabled algorithm to the original DME proposal requiring N copies of ρ_{in} . We label this theoretical process χ_{DME} and calculate the fidelity $F_p(\chi, \chi_{DME})$, shown in dark blue/red. This fidelity combines the physical errors arising from our imperfect gates and the error from using QME to emulate the re-preparation of ρ_{in} . The difference between $F_p(\chi, \chi_{DME})$ and $F_p(\chi, \chi_{ideal})$ is a reflection of finite N error in the underlying DME algorithm.

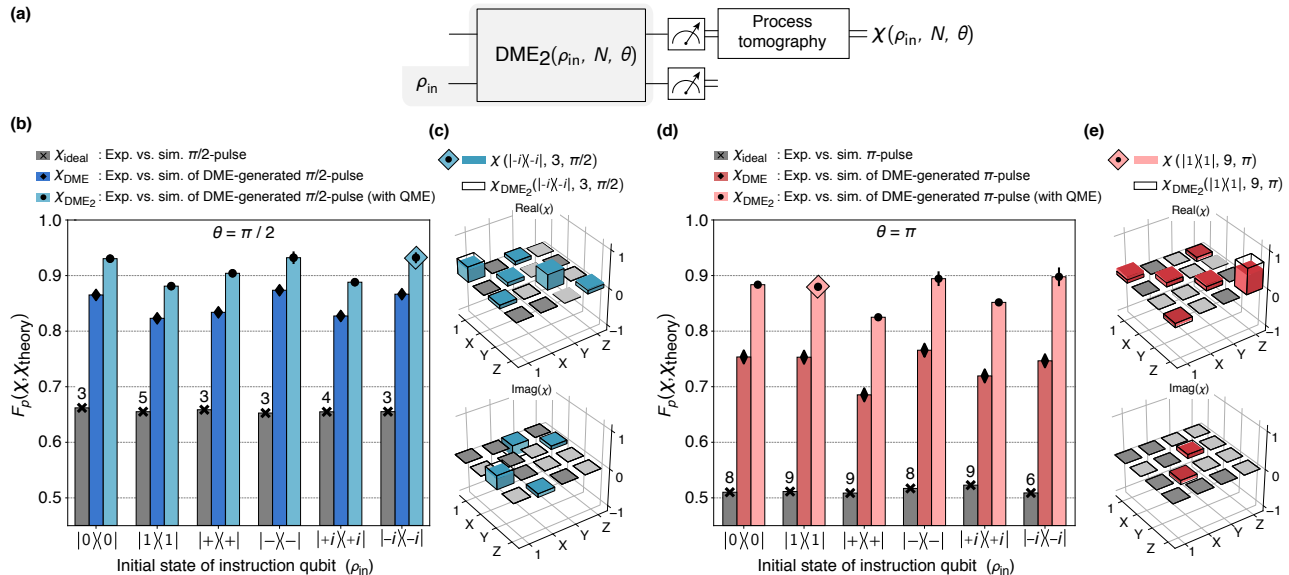


FIG. 4. **Benchmarking algorithmic fidelity of DME_2 .** **(a)** Circuit schematic. Single-qubit process tomography is performed for a set of six instruction states ρ_{in} representing cardinal points of the Bloch sphere. **(b)** **(d)** Process fidelities between measured process maps and simulated processes, for varying instruction state and overall angle in DME_2 . Grey (\times marker) denotes the fidelity $F_p(\chi, \chi_{ideal})$ between the measured process map χ and the ideal process χ_{ideal} , e.g a rotation of angle θ around the axis given by the Bloch vector of ρ_{in} . The data are presented at $N = N_{opt}$, determined as the step-number at which the fidelity to χ_{ideal} is maximized; N_{opt} is indicated by the number above each bar. Dark blue/red (\diamond marker) indicates the fidelity $F_p(\chi, \chi_{DME})$ between the measured process map and a simulated implementation of the DME circuit assuming active reset and reinitialization of the instruction qubit (evaluated at $N = N_{opt}$). Light blue/red (\circ marker) shows the fidelity $F_p(\chi, \chi_{DME_2})$ between the measured process map and a simulation of DME_2 with perfect gates and no decoherence using QME to approximately reinitialize the instruction qubit at each step. Error bars are calculated using bootstrap analysis (see Methods). The process map for the point enclosed by a blue/red diamond is shown in **(c)** **(e)**. **(c)** **(e)** Representative process matrices for χ shown in blue (red) for $\theta = \pi/2$ ($\theta = \pi$), evaluated at N_{opt} . Colored process matrix elements indicate points with magnitude $\chi_{ij} > 0.02$; other elements are grey for clarity of scale. Black wire frames denote a process matrix from a simulated implementation of χ_{DME_2} assuming perfect gate operation and no decoherence.

Finally, we plot the fidelity between our measured process and χ_{DME_2} , a simulated version of the DME_2 algorithm, shown in light blue/red. This fidelity compares the experimental implementation of DME_2 to a classical simulation of DME_2 using perfect operations, and is therefore the most direct metric for the performance of our processor. The theoretical χ_{DME_2} is calculated by sampling all QME randomizations and averaging their effect. The average process fidelity $F_p(\chi, \chi_{DME_2})$ over all instruction settings is 0.91 for $\theta = \pi/2$ and 0.87 for $\theta = \pi$; this algorithmic fidelity is overall reduced for $\theta = \pi$ because N_{opt} occurs at deeper circuit depth.

Outlook

By executing a quantum program whose instructions are stored in a quantum state, we have established the first experimental approach to instilling homoiconicity in quantum computing. The DME_2 algorithm used here to generate quantum instructions takes advantage of a 99.7% fidelity controlled-phase gate combined with a novel simulated quantum measurement technique. We achieve output state fidelities exceeding 0.9 even at circuit depth of 73 sequential

gates and process fidelities close to 0.9, independent of the instruction setting.

Our realization of quantum instructions represents a new approach to quantum computer programming. It uses a fixed set of classical pulses that serve as a program “scaffolding,” and an auxiliary quantum state to encode the program instructions. Intuitively, since the classical scaffolding is always the same, it must be the quantum states that uniquely determine the quantum instructions. While we used pure states to form the quantum instructions in DME_2 , the general DME algorithm generalizes to mixed states and efficiently extends to multi-qubit systems, requiring only the ability to perform controlled versions of the SWAP operation between pairs of target and instruction qubits [8, 9, 28, 40]. Because it bypasses costly and unscalable tomography and recompilation requirements, DME and related algorithms enable exponential speedup for a range of applications spanning quantum state metrology [7], guaranteed private quantum software [9], efficient measurement of large-scale entangled quantum systems [8] and quantum machine learning [41].

END NOTES

Acknowledgements: The authors acknowledge feedback on the manuscript from Antti Vepsäläinen, Cyrus Hirjibehedin, Kyle Serniak, Thomas Hazard, and Steven Weber. MK acknowledges support from the Carlsberg Foundation during part of this work. AG acknowledges funding from the 2019 Google US/Canada PhD Fellowship in Quantum Computing. IM acknowledges funding from NSF grant FET-1910859. This research was funded in part by the U.S. Army Research Office Grant W911NF-18-1-0411 and the Assistant Secretary of Defense for Research & Engineering under Air Force Contract No. FA8721-05-C-0002. Opinions, interpretations, conclusions, and recommendations are those

of the authors and are not necessarily endorsed by the United States Government.

Author contributions: MK, MS, AG, GS, AB, CM, and PK performed the experiments. MK, MS, AG, GS, MO, CM, and KO developed analytical tools and analyzed data. MK, MS, AG, AB, JB, RW, YS, and SG developed experimental control tools. MK, MO, CM, and KO performed algorithm simulations under realistic noise models. MK, MS, AG, GS, MO, MM, DR, SL, and IM developed the DME₂ protocol. DK, AM, BN, and JY fabricated devices. TO, SG, and WO provided experimental oversight and support. All authors contributed to the discussion of the results and the manuscript.

-
- [1] Turing, A. M. On Computable Numbers, with an Application to the Entscheidungsproblem. *Proc. London Math. Soc.* **s2-42**, 230–265 (1937).
- [2] Montanaro, A. Quantum algorithms: an overview. *npj Quantum Information* **2**, 15023 (2016).
- [3] Shor, P. W. Polynomial-Time Algorithms for Prime Factorization and Discrete Logarithms on a Quantum Computer. *SIAM Rev.* **41**, 303–332 (1999).
- [4] DiVincenzo, D. P. Quantum gates and circuits. *Proc. R. Soc. London A* **454**, 261–276 (1998).
- [5] Farhi, E., Goldstone, J., Gutmann, S. & Sipser, M. Quantum Computation by Adiabatic Evolution. *arXiv:quant-ph/0001106* (2000).
- [6] Raussendorf, R. & Briegel, H. J. A One-Way Quantum Computer. *Phys. Rev. Lett.* **86**, 5188–5191 (2001).
- [7] Lloyd, S., Mohseni, M. & Rebentrost, P. Quantum principal component analysis. *Nat. Phys.* **10**, 631–633 (2014).
- [8] Pichler, H., Zhu, G., Seif, A., Zoller, P. & Hafezi, M. Measurement Protocol for the Entanglement Spectrum of Cold Atoms. *Phys. Rev. X* **6**, 041033 (2016).
- [9] Marvian, I. & Lloyd, S. Universal Quantum Emulator. *arXiv:1606.02734* (2016).
- [10] Mooers, C. N., Deutsch, L. P. & Floyd, R. W. Programming languages for non-numeric processing—1: Trac, a text handling language (Association for Computing Machinery, New York, NY, USA, 1965).
- [11] Von Neumann, J. First draft of a report on the edvac. Tech. Rep., University of Pennsylvania (1945).
- [12] Arute, F. *et al.* Quantum supremacy using a programmable superconducting processor. *Nature* **574**, 505–510 (2019).
- [13] Harris, R. *et al.* Phase transitions in a programmable quantum spin glass simulator. *Science* **361**, 162–165 (2018).
- [14] Barz, S. *et al.* Demonstration of Blind Quantum Computing. *Science* **335**, 303–308 (2012).
- [15] Haah, J., Harrow, A. W., Ji, Z., Wu, X. & Yu, N. Sample-Optimal Tomography of Quantum States. *IEEE Transactions on Information Theory* **63**, 5628–5641 (2017).
- [16] Vijay, R. *et al.* Stabilizing rabi oscillations in a superconducting qubit using quantum feedback. *Nature* **490**, 77–80 (2012).
- [17] Riste, D. *et al.* Deterministic entanglement of superconducting qubits by parity measurement and feedback. *Nature* **502**, 350–354 (2013).
- [18] Reed, M. D. *et al.* Realization of three-qubit quantum error correction with superconducting circuits. *Nature* **482**, 382–385 (2012).
- [19] Hu, L. *et al.* Quantum error correction and universal gate set operation on a binomial bosonic logical qubit. *Nature Physics* **15**, 503–508 (2019).
- [20] Ofek, N. *et al.* Extending the lifetime of a quantum bit with error correction in superconducting circuits. *Nature* **536**, 441–445 (2016).
- [21] Campagne-Ibarcq, P. *et al.* Persistent control of a superconducting qubit by stroboscopic measurement feedback. *Phys. Rev. X* **3**, 021008 (2013).
- [22] Andersen, C. K. *et al.* Entanglement stabilization using ancilla-based parity detection and real-time feedback in superconducting circuits. *npj Quantum Information* **5** (2019).
- [23] Preskill, J. Quantum computing in the nisq era and beyond. *Quantum* **2**, 79 (2018).
- [24] Botea, A., Kishimoto, A. & Marinescu, R. On the complexity of quantum circuit compilation. In *Eleventh Annual Symposium on Combinatorial Search* (2018).
- [25] Nielsen, M. A. & Chuang, I. L. Programmable Quantum Gate Arrays. *Physical Review Letters* **79**, 321–324 (1997).
- [26] Ying, M. *Foundations of Quantum Programming* (Elsevier, London, 2016).
- [27] Yuxiang Yang, R. R. & Chiribella, G. Optimal universal programming of unitary gates. *arXiv:2007.10363* (2020). 2007.10363.
- [28] Kimmel, S., Lin, C. Y.-Y., Low, G. H., Ozols, M. & Yoder, T. J. Hamiltonian simulation with optimal sample complexity. *npj Quantum Inf* **3**, 1–7 (2017).
- [29] Brandão, F. G. S. L. *et al.* Quantum SDP Solvers: Large Speed-ups, Optimality, and Applications to Quantum Learning. *arXiv:1710.02581* (2019).
- [30] Salathé, Y. *et al.* Digital quantum simulation of spin models with circuit quantum electrodynamics. *Phys. Rev. X* **5**, 021027 (2015).
- [31] Lloyd, S. Universal Quantum Simulators. *Science* **273**, 1073–1078 (1996).
- [32] Magnard, P. *et al.* Fast and Unconditional All-Microwave Reset of a Superconducting Qubit. *Physical Review Letters* **121**, 060502 (2018).

- [33] Wallman, J. J. & Emerson, J. Noise tailoring for scalable quantum computation via randomized compiling. *Phys. Rev. A* **94**, 052325 (2016).
- [34] Koch, J. *et al.* Charge-insensitive qubit design derived from the Cooper pair box. *Phys. Rev. A* **76**, 042319 (2007).
- [35] Hutchings, M. D. *et al.* Tunable superconducting qubits with flux-independent coherence. *Phys. Rev. Applied* **8**, 044003 (2017).
- [36] Barends, R. *et al.* Coherent Josephson Qubit Suitable for Scalable Quantum Integrated Circuits. *Phys. Rev. Lett.* **111**, 080502 (2013).
- [37] Strauch, F. W. *et al.* Quantum Logic Gates for Coupled Superconducting Phase Qubits. *Phys. Rev. Lett.* **91**, 167005 (2003).
- [38] DiCarlo, L. *et al.* Demonstration of two-qubit algorithms with a superconducting quantum processor. *Nature* **460**, 240–244 (2009).
- [39] Rines, R., Obenland, K. & Chuang, I. Empirical determination of the simulation capacity of a near-term quantum computer. *arXiv:1905.10724* (2019).
- [40] Gao, Y. Y. *et al.* Entanglement of bosonic modes through an engineered exchange interaction. *Nature* **566**, 509–512 (2019).
- [41] Biamonte, J. *et al.* Quantum machine learning. *Nature* **549**, 195–202 (2017).

Supplementary material for “Programming a quantum computer with quantum instructions”

M. Kjaergaard^{†,1,*} M. E. Schwartz,^{2,†} A. Greene,¹ G. O. Samach,^{1,2} A. Bengtsson,^{1,3}
M. O’Keeffe,² C. M. McNally,¹ J. Braumüller,¹ D. K. Kim,² P. Krantz,^{1,‡} M. Marvian,^{1,4}
A. Melville,² B. M. Niedzielski,² Y. Sung,¹ R. Winik,¹ J. Yoder,² D. Rosenberg,² K. Obenland,²
S. Lloyd,^{1,4} T. P. Orlando,¹ I. Marvian,⁵ S. Gustavsson,¹ and W. D. Oliver^{1,2,6,7}

¹*Research Laboratory of Electronics, Massachusetts Institute of Technology, Cambridge, USA, MA 02139*

²*MIT Lincoln Laboratory, 244 Wood Street, Lexington, USA, MA 02421*

³*Microtechnology and Nanoscience, Chalmers University of Technology, Göteborg, Sweden, SE-412 96*

⁴*Department of Mechanical Engineering, Massachusetts Institute of Technology, Cambridge, Massachusetts 02139, USA*

⁵*Departments of Physics & Electrical and Computer Engineering, Duke University, Durham, North Carolina 27708, USA*

⁶*Department of Physics, Massachusetts Institute of Technology, Cambridge, USA, MA 02139*

⁷*Department of Electrical Engineering & Computer Science,
Massachusetts Institute of Technology, Cambridge, USA, MA 02139*

(Dated: December 29, 2020)

CONTENTS

A. Device parameters	1
B. Gate characterization	3
C. Coherent error reduction	5
D. Compilation	6
E. State and process tomography	8
F. Bootstrap error analysis	9
G. Circuit simulation with noise	10
H. Algorithmic error in DME	11
I. Algorithmic error due to QME	13
J. Quantifying the impacts of finite QME randomizations	14
References	15

Appendix A: Device parameters

The quantum processor used in this work has three asymmetric ‘xmon’-style qubits in a linear chain [S1–S3]. We use the two leftmost qubits in this protocol; the third is detuned and idles in its ground state. Extended Data Fig. S1a shows a schematic of the readout- and control- setup used to control the qubits. Extended Data Fig. S1b shows a scanning electron micrograph of a device identical to the one used in this work. In Extended Data Table S1 we summarize the parameters of the two qubits used for the experiments in the main text. The measured lifetime T_1 and Ramsey coherence time T_{2R} exhibit temporal fluctuations, consistent with other reports [S4, S5].

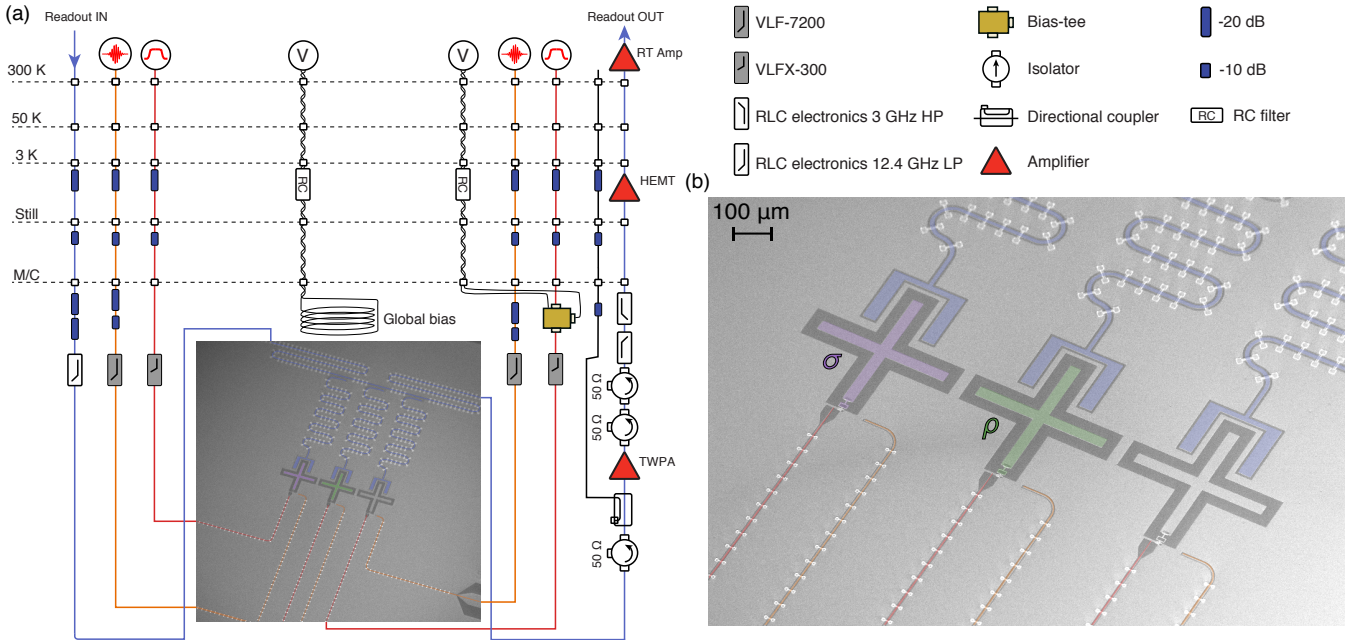
* mortenk@mit.edu

† Authors contributed equally to this work

‡ Current address: Microtechnology and Nanoscience, Chalmers University of Technology

Parameter	Qubit 1 (σ , target)	Qubit 2 (ρ , instruction)
Idling frequency, $\omega_i/2\pi$	4.748 GHz	4.225 GHz
Anharmonicity, $\eta/2\pi$	-175 MHz	-190 MHz
Coupling strength, $g/2\pi$	10.6 MHz	
Readout resonator frequency, $f_i/2\pi$	7.251 GHz	7.285 GHz
Junction asymmetry	1:5	1:10
Relaxation time at idling point, T_1	23 μs	39 μs
Coherence time at idling point, T_{2R}	13 μs	25 μs
Effective relaxation time undergoing CZ trajectory, \tilde{T}_1	$\approx 17 \mu\text{s}$	(same as idling)
Effective coherence time undergoing CZ trajectory, \tilde{T}_{2R}	$\approx 5 \mu\text{s}$	(same as idling)
Single-qubit gate time, $t_{1\text{qb}}$	30 ns	30 ns
Two-qubit gate time, t_{CZ}	60 ns	

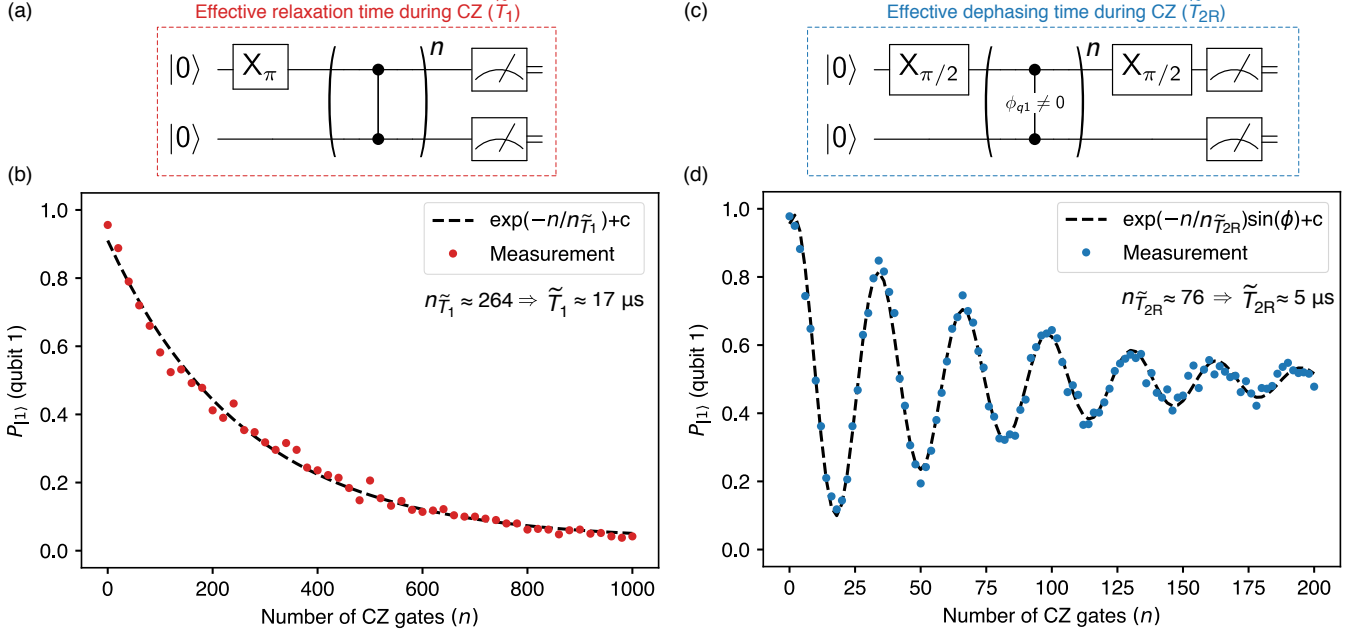
EXTENDED DATA TABLE S1. Parameters of the two qubits used in this work. See text for details of the definition of \tilde{T}_1 and \tilde{T}_{2R} .



EXTENDED DATA FIG. S1. (a) Schematic of readout- and control-wiring used for these experiments. The microwave line of qubit 3 is used to drive single-qubit gates on qubit 2. (b) SEM picture of identically fabricated device to the processor used in this work.

For a qubit undergoing frequency modulation (*e.g.* to implement the CZ gate), frequency-dependent T_1 (and T_{2R}) variations mean that the static coherence times do not necessarily set the relevant limiting time-scale for the qubits [S4]. To account for the frequency-dependent variations in coherence as the target qubit undergoes the CZ trajectory, we employ an *effective* T_1 (T_{2R}) parameter, denoted \tilde{T}_1 (\tilde{T}_{2R}). These effective coherence times take into account any frequency-dependent variations of coherence as the qubit frequency undergoes the trajectory to enact a CZ gate. The effective coherence times are used in simulations of the device performance during two-qubit gates. Since the frequency of qubit 2 is fixed during the CZ gate, its effective coherence times are identical to the idling coherence times.

Extended Data Fig. S2a shows an example measurement of \tilde{T}_1 . We prepare the state $|10\rangle$ (an eigenstate of CZ), apply n CZ gates in sequence, and measure the probability of staying in the $|10\rangle$ state. The exponential decay is fitted and we find a characteristic number of gates, $n_{\tilde{T}_1} \approx 264$. The CZ gate-time is 60 ns, and we use a 5 ns spacing between each pulse, leading to an effective decay time $\tilde{T}_1 = n_{\tilde{T}_1} \cdot t_{\text{CZ}} \approx 17 \mu\text{s}$.



EXTENDED DATA FIG. S2. (a) Measurement circuit to extract effective T_1 -like decay time, denoted \tilde{T}_1 . (b) Probability of measuring qubit 1 in the excited state, as the number of CZ gates is increased. The number $n\tilde{\tau}_1$ sets a characteristic gate number, which can be converted into a characteristic time, \tilde{T}_1 . (c) Measurement circuit to extract effective T_{2R} -like decay time, denoted \tilde{T}_{2R} . We essentially perform a Ramsey measurement, but interleave CZ gates. (d) Probability of measuring qubit 1 in the excited state, as the number of CZ gates is increased. The number $n\tilde{\tau}_{2R}$ gives the effective coherence time $\tilde{T}_{2R} \approx 5 \mu\text{s}$.

To measure the effective coherence time \tilde{T}_{2R} (Extended Data Fig. S2b), we prepare the $|+0\rangle$ state, apply n CZ gates, and apply a final $X_{\pi/2}$ pulse before measuring. Unlike a standard Ramsey measurement, in which we would idle between the $X_{\pi/2}$ pulses, here we perform back-to-back CZ gates, effectively aggregating decoherence effects over the full frequency range of the CZ gate. To ensure an oscillatory behavior, a small single-qubit phase error is added ($\phi_{q1} \neq 0$), equivalent to performing a detuned Ramsey experiment. Fitting an exponentially damped sine function gives a characteristic decay number $n\tilde{\tau}_{2R} \approx 76$ CZ gates. We again estimate the effective coherence time as $\tilde{T}_{2R} = n_{T_{2R}} \cdot t_{CZ} \approx 5 \mu\text{s}$.

Appendix B: Gate characterization

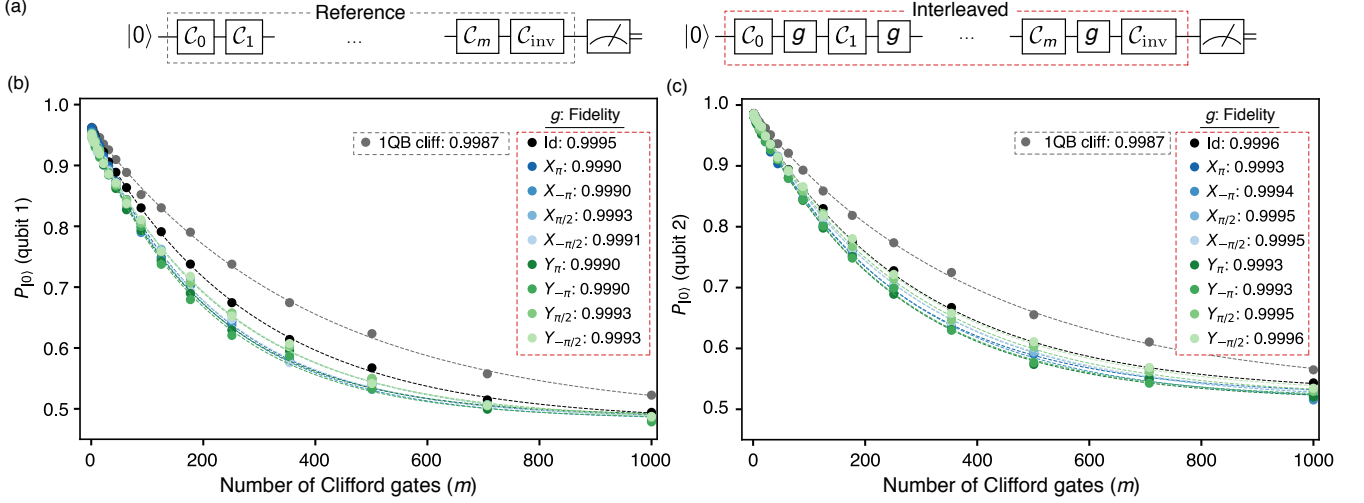
The native gate set of our processor comprises microwave-driven single-qubit x - and y -rotations $R_X(\phi)$ and $R_Y(\phi)$, single-qubit virtual- z rotations $R_Z(\phi)$, and the two-qubit controlled-phase (CZ) gate [S6]. In particular, we calibrate a numerically optimized 99.7% fidelity CZ gate [S7, S8], using the symmetrized ‘NetZero’ optimal control waveform that reduces leakage and noise-sensitivity [S9–S11].

We use a combination of metrics to quantify the quality of qubit operations during the algorithm. These techniques include single- and two-qubit randomized benchmarking (RB) as well as novel techniques for amplifying and correcting coherent errors. Extended Data Fig. S3 shows single-qubit Clifford randomized benchmarking of the single-qubit operations on both qubit 1 (panel b) and 2 (panel c). Each trace averages 25 randomizations of the RB circuit [S12]. The reference curves (circuit diagram in panel a, grey dashed box) are fit to a function of the form

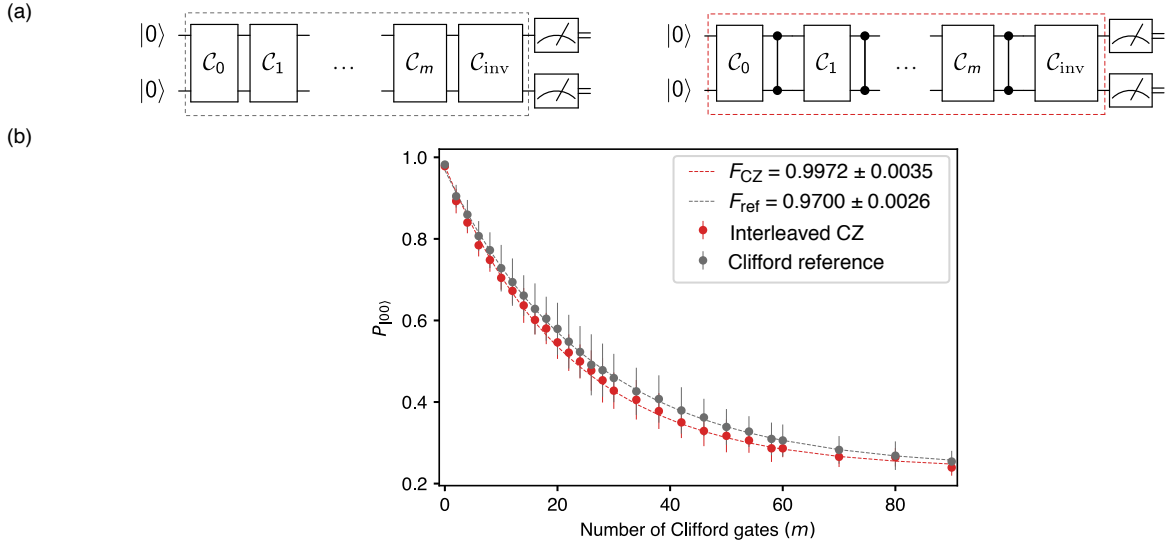
$$f(m) = Ap^m + B \quad (\text{B1})$$

For the one qubit Clifford reference curve we denote p by p_r . The average error per Clifford gate \mathcal{C} can be calculated as

$$\epsilon_r = \frac{1}{2}(1 - p_r) \quad (\text{B2})$$



EXTENDED DATA FIG. S3. (a) Circuit diagrams for measuring the reference curve (gray dashed box) and interleaved curve for a single qubit gate g (red dashed box) relevant for Clifford randomized benchmarking for a single qubit. (b)[(c)] Results for reference (gray) and interleaved (varying colors, for each gate) randomized benchmarking for qubit 1 [qubit 2].



EXTENDED DATA FIG. S4. (a) Gate sequences for measuring the two-qubit Clifford reference (gray dashed box) and interleaved CZ (red dashed box) RB numbers. (b) Example decay curve of $P_{|00\rangle}$ as the number of two-qubit Clifford gates (m) is increased. Each datapoint is averaged over $k = 48$ randomizations of the choice of Clifford gates. Error bars are 1σ standard deviations at each point from the 48 measurements, and fitting is performed using forward propagation of points weighted by their error bars.

The error associated with a specific single-qubit gate is extracted by performing interleaved randomized benchmarking (IRB). We fit the IRB data (circuit diagram in panel a, red dashed box) for the relevant gate (denoted g) to Eq. (B1) (denoting by p_g the p value for gate g). Then normalizing the error rate to the one qubit Clifford reference [S13],

$$\epsilon_g = \frac{1}{2}(1 - p_g/p_r), \quad (\text{B3})$$

Using this procedure we find an average Clifford gate fidelity ($F_r = 1 - \epsilon_r$) of 0.9987 for qubit 1 and 0.9987 for qubit 2. The average gate fidelity (*i.e.* $\bar{F} = \langle 1 - \epsilon \rangle_g$) over all single-qubit gates is 0.9991 for qubit 1 and 0.9994 for qubit 2.

In Extended Data Fig. S4, we assess the two-qubit gate fidelity using randomized benchmarking. The protocol is identical to the single-qubit case, except we measure the probability of being in the $|00\rangle$ state after the sequence [S12]. We use 48 randomizations for both reference and interleaved measurements (circuits shown in panel a). In panel b we show the result of the RB and IRB measurements. The error bars are 1σ standard deviations of the output

distribution of the 48 random circuits. The fit is again performed using Eq. (B1), and error margins are extracted using forward-propagation of weights based on the standard deviation at each m to ensure accurate error bounds. This is achieved using the `absolute_sigma` option of the Python `scipy.optimize.curve_fit` function. The two-qubit Clifford reference error rate is calculated similarly to Eq. (B2) (with p being the two-qubit Clifford reference value, denoted p_{2r}) but the error per Clifford is modified to

$$\epsilon_{2r} = \frac{3}{4}(1 - p_{2r}). \quad (\text{B4})$$

Then, ϵ_{CZ} is found by performing IRB and fitting the interleaved data to get p_{CZ} and normalizing to the 2QB reference error. Doing so, we find a CZ gate fidelity

$$F_{\text{CZ}} = 1 - \epsilon_{\text{CZ}} = 0.9972 \pm 0.0035. \quad (\text{B5})$$

To achieve ‘last-mile’ improvements in fidelity we use numerical optimization techniques to fine-tune parameters of the NetZero waveform, with the RB decay curve as a cost function [S7, S9].

Appendix C: Coherent error reduction

As practitioners of quantum computing have explored more complex circuits at greater depth and with more underlying structure, it has become evident that RB is a limited metric for the performance of a gate (see *e.g.* [S14–S16] and references therein). In particular, small coherent errors can cause disproportionately deleterious effects in algorithms with a repetitive structure (such as Trotterized algorithms), and RB is ill-suited to characterize such small coherent errors because it is designed to randomize over them.

To minimize the effects of coherent errors in the CZ gate, we implement a calibration technique which relies on process tomography of long strings of CZ gates (Extended Data Fig. S5). The general controlled-phase gate (denoted $\text{CZ}_{\phi_{01}, \phi_{10}, \phi_{11}}$) is given by

$$\text{CZ}_{\phi_{01}, \phi_{10}, \phi_{11}} = \begin{bmatrix} 1 & 0 & 0 & 0 \\ 0 & e^{-i\phi_{01}} & 0 & 0 \\ 0 & 0 & e^{-i\phi_{10}} & 0 \\ 0 & 0 & 0 & e^{-i\phi_{11}} \end{bmatrix} \quad (\text{C1})$$

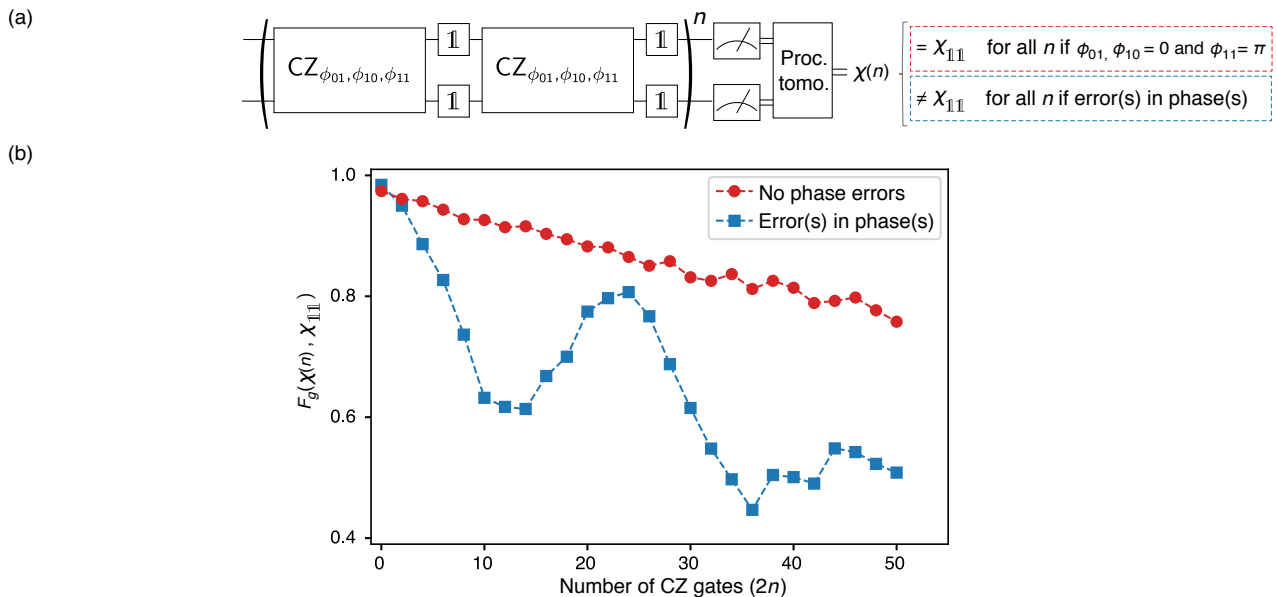
If $\phi_{01} = \phi_{10} = 0$ and $\phi_{11} = \pi$ this produces the target CZ gate. However, for small deviations from these parameters it is still possible to achieve $\gtrsim 0.99$ randomized benchmarking fidelities. Since small phase deviations can compound to form larger errors – specifically in algorithms with a repeating pattern like DME or quantum error correction protocols – we have developed other calibration strategies to detect and correct such errors.

Our amplification protocol is comprised of implementing a circuit with two back-to-back blocks of $\text{CZ}_{\phi_{01}, \phi_{10}, \phi_{11}}$ followed by identity gates on both qubits designed to mimic the presence of single-qubit gates, as shown in Extended Data Fig. S5a. If the CZ gate contains no phase errors, this sequence produces an identity operation, irrespective of the number (n) of such two-CZ blocks applied. We perform two-qubit process tomography to extract the process matrix $\chi(n)$. We compare $\chi(n)$ to the process map of a two-qubit identity operation ($\chi_{\mathbb{1}\mathbb{1}}$) via the gate fidelity $F_g(\chi(n), \chi_{\mathbb{1}\mathbb{1}})$ which is related to the process fidelity (defined in the Methods section ‘‘State and process tomography’’) according to

$$F_g(\chi, \chi') = \frac{dF_p(\chi, \chi') + 1}{d + 1} \quad (\text{C2})$$

where d is the dimensionality of the Hilbert space ($d = 4$ in the case of a two-qubit gate).

Extended Data Fig. S5b shows the gate fidelity of a circuit optimized to remove phase errors from the CZ gate (red circles), and one in which a CZ-gate *with* phase errors is used (blue squares). In the optimized case, the monotonic gate fidelity decay stems only from decoherence effects. However, in the presence of a coherent phase error, the gate fidelity oscillates with n . In this specific example, after roughly 25 CZ gates, the phase-error has effectively rotated by 2π , corresponding to an approximate per-step error of $2\pi/25 \approx 0.08\pi$ in one of the phases. The evolution of the process maps is useful both practically (for achieving higher performance gates) and scientifically (for understanding the limitations of RB). By examining the details of the process maps, we are able to infer in which of the parameters ϕ_{01} , ϕ_{10} or ϕ_{11} the error appeared, and to correct accordingly. This minor correction typically does not change



EXTENDED DATA FIG. S5. (a) Gate sequence used to perform process tomography of a sequence of an even number of CZ gates, to get the chi-matrix $\chi(n)$, used to compare with the identity process map to infer coherent errors. The gate-sequence will nominally implement $\chi_{\mathbb{1}\mathbb{1}}$ up to overall system decoherence (visible as the overall decrease of both the linear and oscillating measurements) if there are no phase errors in the $CZ_{\phi_{01},\phi_{10},\phi_{11}}$ gate. (b) The gate fidelity $F_g(\chi(n), \chi_{\mathbb{1}\mathbb{1}})$ as the number of CZ gates ($2n$) is increased. With no phase errors in the CZ gate, F_g decreases monotonically. With a phase error in the CZ gate F_g will oscillate, with the period indicating the scale of the phase error.

the fidelity as measured with RB (except in the case of particularly egregious phase errors). From Extended Data Fig. S5b it is also clear that process tomography of a single CZ instance does not reveal the coherent error: the first datapoint for the sequence with phase errors has nearly identical fidelity to the optimized gate. Both of these facts are consistent with a growing understanding that RB may not be the optimal approach to identifying and correcting coherent errors in single- and multi-qubit gates. Finally, the identity gates are inserted between the CZ gates to as closely as possible mimic the generic optimal gate-sequence of a two-qubit algorithm, without exploiting any specific structure of an algorithm.

Appendix D: Compilation

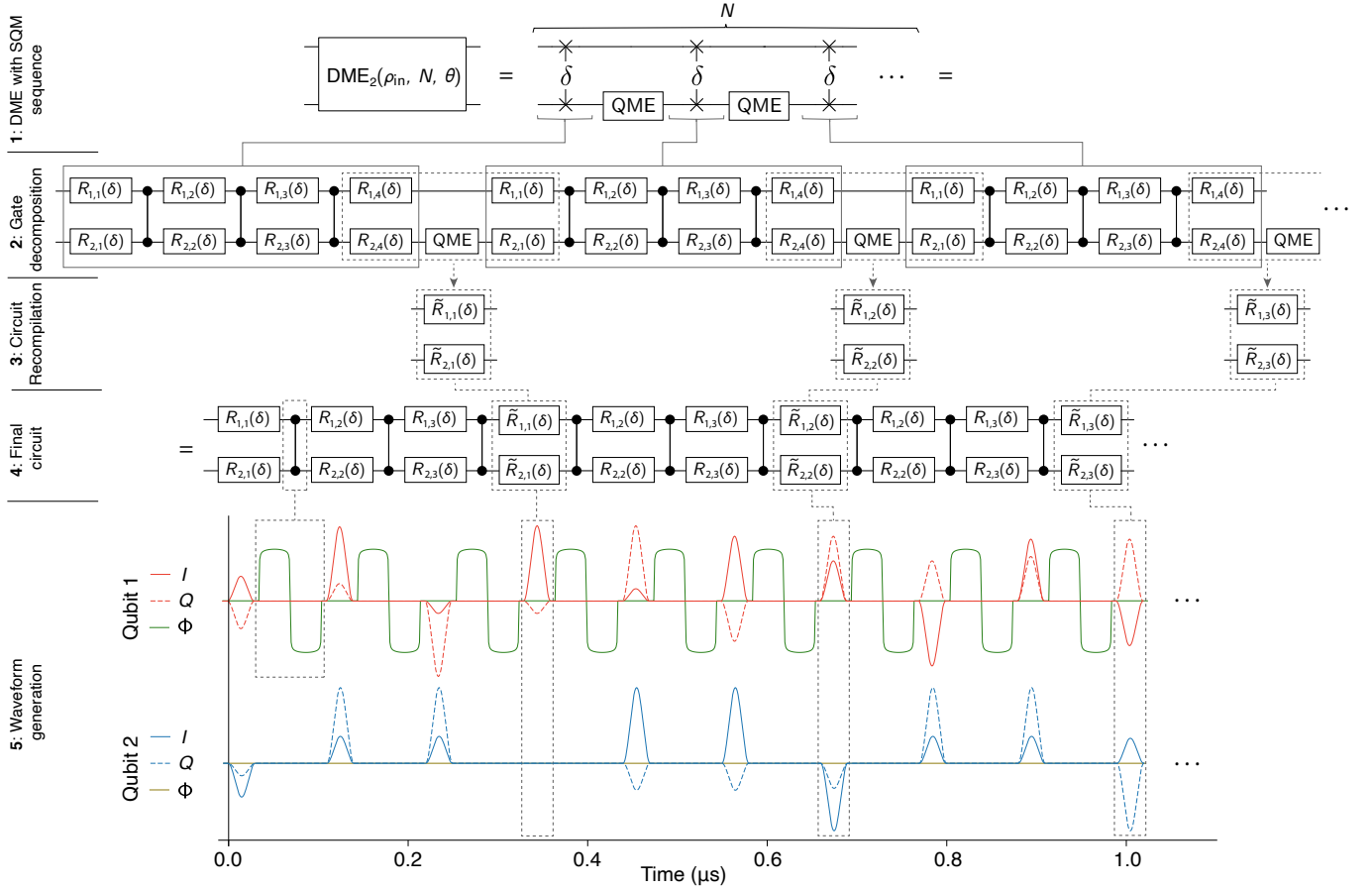
We implement δ SWAP using single-qubit gates and the entangling CZ gate. δ SWAP has an optimal decomposition [S17]

$$\delta\text{SWAP} = \begin{array}{c} \square \\ | \\ \square \end{array} \begin{array}{c} \bullet \\ | \\ \bullet \end{array} \begin{array}{c} \square \\ | \\ \square \end{array} \begin{array}{c} \bullet \\ | \\ \bullet \end{array} \begin{array}{c} \square \\ | \\ \square \end{array} \begin{array}{c} \bullet \\ | \\ \bullet \end{array} \begin{array}{c} \square \\ | \\ \square \end{array} \quad \begin{array}{l} \ast \\ \delta \\ \ast \end{array} \quad (D1)$$

where each \square represents a general single-qubit gate that depends on the value of δ and $\begin{array}{c} \bullet \\ | \\ \bullet \end{array}$ is the CZ gate. The open-source software package Cirq [S18] is used to determine the appropriate single-qubit gate parameters for a given δ SWAP. Our δ SWAP construction allows us to rely solely on high-fidelity gates whose performance can be validated and efficiently optimized.

A conceptually transparent approach to generating a δ SWAP uses the decomposition

$$\delta\text{SWAP} := \begin{array}{c} \bullet \\ | \\ \oplus \end{array} \begin{array}{c} \text{H} \\ | \\ \oplus \end{array} \begin{array}{c} \bullet \\ | \\ \oplus \end{array} \begin{array}{c} \text{H} \\ | \\ \oplus \end{array} \begin{array}{c} \bullet \\ | \\ \oplus \end{array} \quad (D2)$$



EXTENDED DATA FIG. S6. Details of δ SWAP and DME compilation. **Row 1.** The density matrix exponentiation algorithm implemented using partial SWAP operations and the simulated quantum measurement (QME) gate. **Row 2.** Decomposing each δ SWAP according to Eq. (D5). Each substep at this step requires 8 layers of gates (7 for δ SWAP decomposition and 1 for QME). **Row 3.** The three layers of single-qubit gates stemming from the the end of the δ SWAP of step n , followed by QME, and the first layer of single-qubit gates in δ SWAP of step $n + 1$ can be recompiled into a single layer. **Row 4.** The recompiled gates are reinserted into the algorithm result in the optimal structure of exactly one CZ gate, followed by a single layer of single-qubit gates. **Row 5.** Example waveform output to the I, Q (x, y) ports and the flux tuning pulse (labeled Φ) implementing the ‘NetZero’ waveform used to implement the CZ gate [S9, S10].

where

$$\begin{array}{c} \bullet \\ | \\ \delta \\ | \\ \bullet \end{array} = \begin{pmatrix} 1 & 0 & 0 & 0 \\ 0 & 1 & 0 & 0 \\ 0 & 0 & 1 & 0 \\ 0 & 0 & 0 & e^{-i\delta} \end{pmatrix} := \text{CZ}_\delta \quad (\text{D3})$$

is a partial CZ gate and $\begin{array}{c} \bullet \\ | \\ \oplus \\ | \\ \bullet \end{array}$ is the CNOT gate with qubit 2 as the target. The CZ_δ gate can in turn be compiled using an additional decomposition

$$\begin{array}{c} \bullet \\ | \\ \delta \\ | \\ \bullet \end{array} = \begin{array}{c} \boxed{Z_{\delta/2}} \\ | \\ \boxed{Z_{\delta/2}} \oplus \boxed{Z_{-\delta/2}} \end{array} \quad (\text{D4})$$

However, such an approach would introduce two CZ gates for each CZ_δ gate, adding significant circuit depth overhead. We use a more generalized and gate-efficient approach, relying on the fact that any two-qubit gate can generically be decomposed into a circuit with the structure [S17, S19]

$$U_{2\text{QB}} = \begin{array}{c} \boxed{R_{1,1}} \bullet \boxed{R_{1,2}} \bullet \boxed{R_{1,3}} \bullet \boxed{R_{1,4}} \\ | \\ \boxed{R_{2,1}} \oplus \boxed{R_{2,2}} \oplus \boxed{R_{2,3}} \oplus \boxed{R_{2,4}} \end{array} \quad (\text{D5})$$

Here $R_{i,j}$ is a single-qubit gate acting on qubit i at moment j in the circuit.

By using the identity



$$\text{CNOT}_{1,2} = \text{H}_2 \text{CNOT}_{2,1} \text{H}_2 \quad (\text{D6})$$

and absorbing the Hadamard gates (H) into the neighboring single-qubit gates, the circuit in Eq. (D5) becomes identical to the circuit in Eq. (D1).

We use the open-source software `Cirq` [S18] to determine the settings of the single-qubit gates for each value of δ . The single-qubit rotations around the x, y axes are decomposed according to $R_Z(-\varphi)R_X(\theta)R_Z(\varphi)$ (the `PhasedXPowGate` in `Cirq`) and the R_Z rotations are performed virtually [S20]. The δ SWAP is implemented using the `SwapPowGate` function in `Cirq` (the `SwapPowGate` has a factor of 2 difference, relative to our definition of δ SWAP). Thus, we are able to compose a unique composite gate sequence for each δ SWAP relying only on high-fidelity single- and two-qubit gates.

Extended Data Fig. S6 shows the full compilation protocol. To construct the full $\text{DME}(\rho, N, \theta)$ circuit, we append N copies of the compiled δ SWAP gate using $\delta = \theta/N$, interleaving the requisite QME_ν on qubit 2 (the instruction qubit, ρ) to emulate the effect of measurements. Rows 1 and 2 show the generic structure and gate decomposition of our implementation of DME_2 . The final layer of single-qubit gates in the δ SWAP at step n can be recompiled together with the QME_ν and the first layer of single-qubit gates in the δ SWAP at step $n+1$. We use `Cirq` to slice out these three layers (Row 2) of single-qubit gates, recompile them into a single layer (Row 3), and reinsert them (Row 4). Finally, in Row 5 we show an example waveform output from our signal generation software, implementing the first $n=3$ steps in a $N=5$ DME_2 program.

Our compilation relies upon a restricted set of gates that are readily characterized and numerically optimized. The final compiled circuit has a regular structure (each CZ is followed by exactly one layer of single-qubit gates), amenable to generic tuneup protocols for reducing coherent error buildup. These features enable it to achieve high algorithmic fidelity at significant circuit depth.

Appendix E: State and process tomography

Quantum state tomography is performed by taking advantage of independent single-shot readout of all four computational states $\{00, 01, 10, 11\}$. We first calibrate the measurement operators by building a matrix $\bar{\beta}$ that maps the two-qubit Pauli matrices $\hat{\sigma}_{11}, \hat{\sigma}_{1Z}, \hat{\sigma}_{Z1}$, and $\hat{\sigma}_{ZZ}$ onto the measurement probabilities p_{ij} :

$$\vec{p} = \bar{\beta} \vec{\sigma}, \quad (\text{E1})$$

where

$$\vec{p} \equiv \begin{pmatrix} p_{00} \\ p_{01} \\ p_{10} \\ p_{11} \end{pmatrix} \quad \text{and} \quad \vec{\sigma} \equiv \begin{pmatrix} \hat{\sigma}_{11} \\ \hat{\sigma}_{1Z} \\ \hat{\sigma}_{Z1} \\ \hat{\sigma}_{ZZ} \end{pmatrix} \quad (\text{E2})$$

The $\bar{\beta}$ matrix is calibrated using techniques drawn from Ref. [S21]; a full motivation and derivation of the technique can be found there. For a measurement of \vec{p} with perfect fidelity and no qubit decay during measurements, all components of $\bar{\beta}$ have amplitude 0.25; deviations from this amplitude correspond to a calibration of such measurement errors. We begin by calibrating the single-qubit $\bar{\beta}$ matrices, namely

$$\begin{pmatrix} p_0 \\ p_1 \end{pmatrix} = \begin{pmatrix} \beta_1^0 & \beta_Z^0 \\ \beta_1^1 & \beta_Z^1 \end{pmatrix} \begin{pmatrix} \hat{\sigma}_1 \\ \hat{\sigma}_Z \end{pmatrix} \quad (\text{E3})$$

by fitting Rabi oscillations in p_0 and p_1 for each qubit. Because the two-qubit probability vector \vec{p} is generated from correlations between single-qubit measurements, the two-qubit $\bar{\beta}$ matrix is given by the tensor product of the single-qubit matrices, *e.g.* $\bar{\beta} = \bar{\beta}_1 \otimes \bar{\beta}_2$.

An arbitrary 4×4 matrix, including a two-qubit density matrix ρ , may be mapped onto the Pauli basis according to

$$\rho = \sum_{i,j=\{1,X,Y,Z\}} c_{ij} \hat{\sigma}_{ij}. \quad (\text{E4})$$

The general 4×4 matrix of this form has sixteen degrees of freedom; trace normalization of a physical density matrix reduces this to fifteen. The native readout gives us access to the components of ρ contained in $\hat{\sigma}_Z$. We gain information about the other components by performing one of nine pre-measurement rotations drawn from:

$$R = R_1 \otimes R_2 \quad (\text{E5})$$

where

$$R_{1,2} = \begin{cases} R_Y(-\frac{\pi}{2}) & \text{mapping } \hat{\sigma}_X \mapsto \hat{\sigma}_Z \\ R_X(\frac{\pi}{2}) & \text{mapping } \hat{\sigma}_Y \mapsto \hat{\sigma}_Z \\ \mathbb{1} & \text{mapping } \hat{\sigma}_Z \mapsto \hat{\sigma}_Z \end{cases} \quad (\text{E6})$$

For data in Figure 2 (3, 4) we perform 2000 (500) single-shot measurements for each tomographic rotation in order to ensure accurate estimates of \vec{p} . Each of the nine rotation-and-measurement pairings provides four linearly independent measurements of a form similar to Eq. (E1), for a total of thirty-six equations that over-specify fifteen degrees of freedom. We perform maximum-likelihood estimation [S22] to derive the positive semi-definite Hermitian matrix that is most consistent with our combined measurement results.

Single-qubit density matrices in Figures 2–3 are extracted by performing partial traces over the two-qubit density matrix calculated using the approach described above; the data in Figure 4 are drawn from single-qubit tomography performed on the target qubit using a similar protocol.

Single-qubit quantum process tomography, as presented in Figure 4, is performed using standard techniques [S19]. The target qubit is sequentially prepared in four input states

$$\sigma_{\text{in}} = \{|0\rangle\langle 0|, |1\rangle\langle 1|, |+\rangle\langle +|, |i\rangle\langle i|\} \quad (\text{E7})$$

which span the single-qubit Hilbert space. These prepared states are then passed through the process $\text{DME}_2(\rho_{\text{in}}, N, \theta)$ and single-qubit state tomography is performed to extract the set of mappings $\{\sigma_{\text{in}} \xrightarrow{\text{DME}_2(\rho_{\text{in}}, N, \theta)} \sigma(N)\}$. Linear combinations of these mappings provide the process map χ that reveals the effect of the quantum channel on an arbitrary input density matrix. We then employ techniques developed in Ref. [S23] to efficiently project χ onto the closest completely positive and trace-preserving (CPTP) mapping χ_{CPTP} , ensuring physicality of the process.

Appendix F: Bootstrap error analysis

We employ bootstrapping techniques to derive the uncertainty bounds in Figs. 3–4. In principle, one could simply take a sample of many QME randomizations and calculate the mean and uncertainty within that dataset. However, those error bars are not representative of the error in the DME_2 protocol – rather, they represent the uncertainty of a protocol in which only a single QME randomization is used to perform DME_2 . As a result, these error bars are unphysically large, particularly at small N where the protocol chooses from one of only a few paths that have very different outcomes.

The true uncertainty of the DME_2 protocol is captured by *i*) accumulating enough QME samples to ensure sufficient randomizations, *ii*) building density/process matrices from the average outcome of all these randomizations, and then *iii*) repeating this process many times with different randomizations to estimate the uncertainty. This is precisely what bootstrapping accomplishes [S24].

The following describes the protocol for extracting bootstrapped averages and uncertainties for Figure 3. For each data point representing a unique setting of $\text{DME}_2(\rho_{\text{in}}, N, \theta)$, we employ the following protocol:

1. For a given instantiation of the QME gates, execute $\text{DME}_2(\rho_{\text{in}}, N, \theta)$ and perform two-qubit state tomography.
2. For r_{QME} different instantiations of QME gates, repeat step 1 to accumulate the experimental density matrices from which bootstrapped samples will be drawn.

3. Using sample-with-replacement, select n_{samp} samples from the r_{QME} datasets and average the density matrices together. This represents a single bootstrapped density matrix.
4. Perform a partial trace over the instruction qubit to extract the reduced density matrix of the target system.
5. Calculate the state fidelity to the states of interest.
6. Repeat steps 3-5 a total of N_{samp} times to extract mean fidelities and 1σ uncertainties.

State fidelity is calculated according to [S25]

$$F_s(\sigma, \sigma') = \text{Tr} \left(\sqrt{\sqrt{\sigma'} \sigma \sqrt{\sigma'}} \right)^2. \quad (\text{F1})$$

The bootstrapping protocol for generating process maps and process fidelities in Figure 4 is similar to that used for state tomography, but we lay it out here explicitly for completeness.

1. For a given instantiation of the QME gates, prepare the target input states $\{\sigma_{\text{in}}\}$, apply $\text{DME}_2(\rho_{\text{in}}, N, \theta)$, and perform single-qubit state tomography to generate the mappings $\{\sigma_{\text{in}} \mapsto \sigma(N)\}$ required for process tomography.
2. For r_{QME} different instantiations of QME gates, repeat step 1 to produce a set of $4 \times r_{\text{QME}}$ single-qubit density matrices.
3. For each of the four σ_{in} , select an independent sample-with-replacement of n_{samp} σ_{out} instances and average together, leaving four averaged mappings $\{\sigma_{\text{in}} \mapsto \sigma_{\text{out}}\}$.
4. Calculate the process matrix using the averaged mappings $\sigma_{\text{in}} \mapsto \sigma(N)$. This represents a single bootstrapped process matrix.
5. Calculate the process fidelity to the process of interest.
6. Repeat steps 3-5 a total of N_{samp} times to extract mean fidelities and 1σ uncertainties.

The process fidelity between two χ -matrices is given by [S26]:

$$F_p(\chi, \chi') = \text{Tr} \left(\sqrt{\sqrt{\chi'} \chi \sqrt{\chi'}} \right)^2. \quad (\text{F2})$$

In Figure 3 we collect $r_{\text{QME}} = 295$ circuit randomizations; in Figure 4 we collect $r_{\text{QME}} = 105$ circuit randomizations. In both cases we use $n_{\text{samp}} = 100$ and $N_{\text{samp}} = 50$. The number of QME randomizations used for process tomography was limited by experimental time, due to the significant additional experimental overhead required for process tomography in comparison to state tomography, and due to the fact that in Figure 4 we characterize processes for six settings of ρ . The bootstrap sample size n_{samp} and number of bootstrap samples N_{samp} are chosen somewhat arbitrarily, as in all bootstrapping implementations, but are designed to ensure that each bootstrapped sample approaches a central limit with respect to the underlying QME randomization. A graphical representation of the convergence under QME randomizations is shown in Extended Data Fig. S8; more details are provided in the Supplementary Methods.

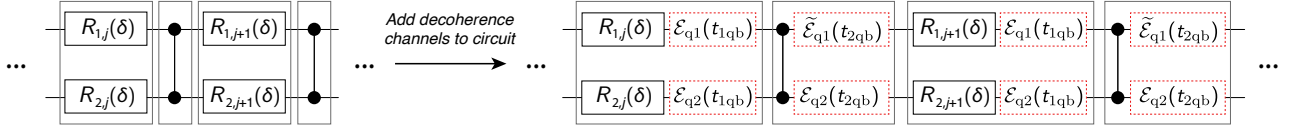
Appendix G: Circuit simulation with noise

In order to show the qualitative consistency between the data in Figure 3 and a model of coherence-limited implementation of the DME_2 protocol, we simulate the randomized DME_2 circuits with added decoherence. We input a DME_2 circuit generated by Cirq to a software tool that adds decoherence (amplitude damping and dephasing) channels corresponding to the identity for duration(s) of the preceding one- or two-qubit gate. An example of this procedure is shown in Extended Data Fig. S7.

The channel \mathcal{E} that composes amplitude damping and dephasing is given by

$$\mathcal{E}_{qk}(t_{1\text{qb}}) : \rho_{qk} \mapsto \sum_{\substack{i=1,2 \\ j=1,2,3}} A_{i,\Gamma_1}(t_{1\text{qb}}) D_{j,\Gamma_\phi}(t_{1\text{qb}}) \rho_{qk} D_{j,\Gamma_\phi}^\dagger(t_{1\text{qb}}) A_{i,\Gamma_1}^\dagger(t_{1\text{qb}}), \quad (\text{G1})$$

where $A_{i,\Gamma_1}(t)$ is the amplitude damping process (with $\Gamma_1 = 1/T_1$), and $D_{j,\Gamma_\phi}(t)$ is the dephasing process ($\Gamma_\phi = 1/T_{2R} - 1/2T_1$), $\Gamma_{1,qk}$ and $\Gamma_{\phi,qk}$ are the appropriate coherence parameters for qubit k , and t is the time of

EXTENDED DATA FIG. S7. Instrumenting the DME₂ circuit for simulation of decoherence-induced errors.

the preceding single- or two-qubit gate on that qubit. The amplitude damping and dephasing Krauss operators are given by

$$A_{1,\Gamma_1}(t) = \begin{pmatrix} 1 & 0 \\ 0 & e^{-\Gamma_{1,qk}t/2} \end{pmatrix}, \quad (\text{G2})$$

$$A_{2,\Gamma_1}(t) = \begin{pmatrix} 0 & \sqrt{1 - e^{-\Gamma_{1,qk}t}} \\ 0 & 0 \end{pmatrix}, \quad (\text{G3})$$

$$D_{1,\Gamma_\phi}(t) = \begin{pmatrix} e^{-\Gamma_{\phi,qk}t/2} & 0 \\ 0 & e^{-\Gamma_{\phi,qk}t/2} \end{pmatrix}, \quad (\text{G4})$$

$$D_{2,\Gamma_\phi}(t) = \begin{pmatrix} \sqrt{1 - e^{-\Gamma_{\phi,qk}t}} & 0 \\ 0 & 0 \end{pmatrix}, \quad (\text{G5})$$

$$D_{3,\Gamma_\phi}(t) = \begin{pmatrix} 0 & 0 \\ 0 & \sqrt{1 - e^{-\Gamma_{\phi,qk}t}} \end{pmatrix}. \quad (\text{G6})$$

The channel $\tilde{\mathcal{E}}$ is defined similarly to \mathcal{E} , but decoherence rates in the process definitions are replaced with their *effective* coherence parameters. The channel $\tilde{\mathcal{E}}$ thus accounts for the modified coherence properties as qubit 1 undergoes the CZ trajectory (see Extended Data Fig. S2).

Each instrumented circuit yields an QME-dependent density matrix representing the simulated finite-coherence circuit output for that QME realization. These density matrices are averaged over all 2^N QME realizations (for a DME₂ circuit with N steps), thus producing the ‘noisy’ simulated two-qubit DME₂ output state, denoted ‘Sim. $F_s(\sigma, \sigma_{\text{ideal}})$ with decoherence’ and plotted as a solid line in Figure 3b. For the simulations presented, we used parameters $T_1 = 20 \mu\text{s}$, $T_{2R} = 10 \mu\text{s}$ for both qubits, and effective coherence times for qubit 1 of $\tilde{T}_1 = 10 \mu\text{s}$ and $\tilde{T}_{2R} = 5 \mu\text{s}$ during the channel $\tilde{\mathcal{E}}$. These parameters are qualitatively consistent with, but overall reduced from, the measured parameters in Table S1. This difference may indicate additional coherent errors not captured by this model (e.g. from residual $\hat{\sigma}_Z \hat{\sigma}_Z$ -interaction or leakage out of the computational subspace).

Appendix H: Algorithmic error in DME

In this section we show that the algorithmic error in DME(ρ, N, θ) (the version of DME in which the instruction state is refreshed with a new, perfect copy after each Trotter step) may be modeled as an amplitude damping channel and derive its scaling with the parameters of the algorithm. We do so first for a specific instruction state, and then generalize to an arbitrary instruction. Throughout we use $\hat{\sigma}_i$ to indicate the corresponding Pauli matrix.

Suppose that we have instruction and target qubits initially in states ρ and σ respectively, and apply the operation $e^{-i\text{SWAP}\delta}$ to the joint state $\rho \otimes \sigma$. We will first consider the special case in which $\rho = |0\rangle\langle 0|$ and then show how this generalizes to an arbitrary state. The effect of the δSWAP on the target qubit is given by the quantum channel

$$\mathcal{E}_{\delta\text{SWAP}}^{\rho=|0\rangle\langle 0|}(\sigma) = \text{Tr}_\rho \left(e^{-i\text{SWAP}\delta} \left[\sigma \otimes |0\rangle\langle 0| \right] e^{i\text{SWAP}\delta} \right), \quad (\text{H1})$$

Next, we use the fact that

$$e^{i\text{SWAP}\delta} = \cos(\delta)\hat{\sigma}_{\mathbb{1}\mathbb{1}} + i \sin(\delta)\text{SWAP}, \quad (\text{H2})$$

which follows from the fact that $\text{SWAP}^2 = \hat{\sigma}_{\mathbb{1}\mathbb{1}}$ where $\hat{\sigma}_{\mathbb{1}\mathbb{1}}$ is the two-qubit identity matrix. Using this together with the identity $\text{Tr}_\rho(\text{SWAP}(X \otimes Y)) = YX$ (where Tr_ρ is a partial trace over the second subsystem) we find

$$\mathcal{E}_{\delta\text{SWAP}}^{\rho=|0\rangle\langle 0|}(\sigma) = \cos^2(\delta)\sigma + i \cos(\delta) \sin(\delta)[\sigma, |0\rangle\langle 0|] + \sin^2(\delta) |0\rangle\langle 0|. \quad (\text{H3})$$

Using the matrix representation of σ in the $\{|0\rangle, |1\rangle\}$ basis, we find that σ transforms as

$$\begin{pmatrix} \sigma'_{00} & \sigma'_{01} \\ \sigma'_{10} & \sigma'_{11} \end{pmatrix} = \begin{pmatrix} \sigma_{00} + \sigma_{11} \sin^2(\delta) & \cos \delta e^{-i\delta} \sigma_{01} \\ \cos \delta e^{+i\delta} \sigma_{10} & \sigma_{11} \cos^2(\delta) \end{pmatrix} \quad (\text{H4})$$

where $\sigma_{ij} = \langle i|\sigma|j\rangle$ as measured in the $\{|0\rangle, |1\rangle\}$ basis. The channel that implements this transformation has a simple interpretation as the composition of a rotation and an amplitude decay.

Let

$$\mathcal{U}_\delta^{\rho=|0\rangle\langle 0|}(\cdot) = e^{-i\delta|0\rangle\langle 0|}(\cdot)e^{i\delta|0\rangle\langle 0|} = e^{-i\frac{\delta}{2}\hat{\sigma}_z}(\cdot)e^{+i\frac{\delta}{2}\hat{\sigma}_z} \quad (\text{H5})$$

be the superoperator corresponding to the unitary $e^{-i\delta|0\rangle\langle 0|}$, or equivalently, the superoperator corresponding to the rotation by angle δ around z axis. Also, let \mathcal{A}_p be the amplitude damping channel described by the Kraus decomposition

$$\mathcal{A}_p(\sigma) = A_1\sigma A_1^\dagger + A_2\sigma A_2^\dagger \quad (\text{H6})$$

where

$$A_1 = \begin{pmatrix} 1 & 0 \\ 0 & \sqrt{1-p} \end{pmatrix}, \quad A_2 = \begin{pmatrix} 0 & \sqrt{p} \\ 0 & 0 \end{pmatrix}. \quad (\text{H7})$$

This amplitude damping channel describes the process in which the system in state $|1\rangle$ decays to state $|0\rangle$ with probability p . It can be shown that the amplitude damping channel satisfies the condition

$$\mathcal{A}_p \circ \mathcal{U}_\delta = \mathcal{U}_\delta \circ \mathcal{A}_p \quad (\text{H8})$$

for all $\theta \in [0, 2\pi)$. This equality implies that the action of this channel is invariant under rotations around z axis.

Then, using Eq. (H4) one can show that

$$\mathcal{E}_{\delta\text{SWAP}}^{\rho=|0\rangle\langle 0|}(\sigma) = \mathcal{A}_{\sin^2(\delta)} \circ \mathcal{U}_\delta(\sigma) = \mathcal{U}_\delta \circ \mathcal{A}_{\sin^2(\delta)}(\sigma) \quad (\text{H9})$$

The overall effect of one Trotter step of DME_N can therefore be understood as the following: (i) Applying the unitary $e^{-i\delta|0\rangle\langle 0|}$ to the system σ , followed by (ii) applying the amplitude damping channel $\mathcal{A}_{\sin^2 \delta}$ to the system σ . Note that because of the condition in Eq. (H8), by flipping the order of steps (i) and (ii) we get exactly the same final state.

Now suppose we repeat the above operation N times. That is we prepare the instruction qubit in state $\rho = |0\rangle\langle 0|$, couple it to σ via the unitary $e^{-i\text{SWAP}\delta}$, then discard the instruction qubit and prepare it again in state $|0\rangle\langle 0|$, and repeat the above procedure with N different copies of ρ . Then, using Eq. (H8) one can show that, given an initial state σ , the final state of the target system will be

$$\left[\mathcal{E}_{\delta\text{SWAP}}^{\rho=|0\rangle\langle 0|} \right]^N(\sigma) = \left[\mathcal{A}_{\sin^2(\delta)} \circ \mathcal{U}_\delta \right]^N(\sigma) = \mathcal{A}_{\sin^2(\delta)}^N \circ \mathcal{U}_{N\delta}(\sigma). \quad (\text{H10})$$

Since amplitude damping channels are closed under composition, we see that

$$\mathcal{A}_{\sin^2(\delta)}^N = \mathcal{A}_{1-\cos^2 N(\delta)}. \quad (\text{H11})$$

Therefore, the overall effect on the target system is equivalent to applying the perfect unitary $e^{-iN\delta|0\rangle\langle 0|}$, and then applying the amplitude damping channel $\mathcal{A}_{1-\cos^2 N(\delta)}$.

Now, suppose in the above procedure, instead of state $|0\rangle\langle 0|$ we prepare the instruction qubit in state $|\phi\rangle\langle\phi| = V|0\rangle\langle 0|V^\dagger$, where V is an arbitrary unitary. Then, using the fact that $\text{SWAP}(V \otimes V') = (V' \otimes V)\text{SWAP}$, one can show that the overall effect of this transformation on the target system can be described as a unitary rotation $e^{-iN\delta|\phi\rangle\langle\phi|}$ followed by an amplitude damping channel in the basis defined by state $|\phi\rangle$ and its orthogonal state.

To translate explicitly to the language of the main text, let $\delta = \theta/N$ and $\rho = |\phi\rangle\langle\phi|$, and use the above procedure to implement the unitary $e^{-i\rho\theta}$ on the target system σ , using N copies of the instruction state ρ . From Eq. (H11) we find that the overall error in this procedure is determined by the probability $p_N = 1 - \cos^2 N(\delta)$. Then, for $\delta \in (0, 2\pi]$ and $N \gg 1$ we have

$$p_N = 1 - \cos^2 N \left(\frac{\theta}{N} \right) \approx 1 - e^{-\frac{\theta^2}{N}} \approx \frac{\theta^2}{N}, \quad \text{for large } N \quad (\text{H12})$$

In the limit of large N , this corresponds to an algorithmic error for the DME_N algorithm of $\mathcal{O}(\theta^2/N)$, as quoted in the main text.

Appendix I: Algorithmic error due to QME

Here we provide an intuitive picture for the quantum measurement emulation (QME) operation as well as a formal proof of the modified algorithmic error bound in Eq. (4) of the main paper.

We will build the intuition for this section by returning to the concrete example from Appendix H, *i.e.* the instruction qubit prepared in $\rho = |0\rangle\langle 0|$. We will also suppose that the target qubit is prepared in an orthogonal state, say, $\sigma = |+i\rangle\langle +i|$ (which is an eigenstate of the Pauli matrix $\hat{\sigma}_Y$). Since δ SWAP is a symmetric operation by the logic in Appendix H the state of ρ following a small δ SWAP interaction is given by a rotation about the y -axis followed by an amplitude damping channel (which we will neglect for the moment). In this case, the state of the instruction qubit becomes

$$\rho' = \begin{pmatrix} \cos^2(\delta) & -\cos(\delta)\sin(\delta) \\ -\cos(\delta)\sin(\delta) & \sin^2(\delta) \end{pmatrix} \quad (I1)$$

The trace distance between ρ and ρ' is of order $|\delta|$. However, if we measure-and-forget the state of the instruction qubit in the basis of its original polarization (*i.e.* the z -basis), the coherent off-diagonal components of the density matrix are dephased and we are left with

$$\rho'' = \begin{pmatrix} \cos^2(\delta) & 0 \\ 0 & \sin^2(\delta) \end{pmatrix} \quad (I2)$$

The trace distance between ρ'' and ρ is of order δ^2 . Because DME operates in the $\delta \ll 1$ regime, we have $\delta^2 \ll \delta$. Measuring-and-forgetting therefore leaves the instruction qubit in a slightly perturbed state that is closer to that of the initial state ρ .

The intuition developed for $\rho = |0\rangle\langle 0|$ extends naturally to an arbitrary initial state $\rho = |\nu_{\parallel}\rangle\langle \nu_{\parallel}|$, in a basis defined by $\nu = \{|\nu_{\parallel}\rangle, |\nu_{\perp}\rangle\}$. A small arbitrary rotation will result in the state

$$\rho' = \cos^2(\beta) |\nu_{\parallel}\rangle\langle \nu_{\parallel}| + \sin^2(\beta) |\nu_{\perp}\rangle\langle \nu_{\perp}| + \cos(\beta)\sin(\beta) (e^{i\phi} |\nu_{\parallel}\rangle\langle \nu_{\perp}| + e^{-i\phi} |\nu_{\perp}\rangle\langle \nu_{\parallel}|), \quad (I3)$$

where β and ϕ generically parameterize the rotation. A measurement in the basis ν dephases the off-diagonal elements in this basis, leaving

$$\rho'' = \cos^2(\beta) |\nu_{\parallel}\rangle\langle \nu_{\parallel}| + \sin^2(\beta) |\nu_{\perp}\rangle\langle \nu_{\perp}| \quad (I4)$$

which is closer than ρ' to ρ by a factor of $|\beta|$.

Performing a physical measurement along an arbitrary axis ν generically would require *i*) rotating ν onto the z -axis, *ii*) performing a projective readout, and *iii*) rotating back to the original axis. All of these steps require finite clock time: single-qubit gates (measurements) typically require tens (hundreds) of nanoseconds to complete. We would like to avoid this significant experimental overhead while still maintaining the ability to partially restore the instruction qubit to its initial state. Instead of physically performing the measurement, we can apply the unitaries $\{\hat{\sigma}_{\mathbf{1}}, \hat{\sigma}_{\nu}\}$ with equal probabilities, where $\hat{\sigma}_{\nu} = \hat{n}_{\parallel} \cdot (\hat{\sigma}_X, \hat{\sigma}_Y, \hat{\sigma}_Z)$ and \hat{n}_{\parallel} is a unit vector parallel to ρ . Such protocols may be equivalently thought of as an approach to turning a coherent error into an incoherent error along a known axis. This protocol is the quantum measurement emulation (QME) operation used in the main paper.

When averaged over many iterations, the randomized QME operation dephases the system in the ν basis, just as in Eq. (I3)-(I4). Assuming the instruction qubit is initially in state ρ' , it turns out that the resulting state is the same for measurement and random gate application, *i.e.*

$$\frac{|\nu_{\parallel}\rangle\langle \nu_{\parallel}| \rho' |\nu_{\parallel}\rangle\langle \nu_{\parallel}| + |\nu_{\perp}\rangle\langle \nu_{\perp}| \rho' |\nu_{\perp}\rangle\langle \nu_{\perp}|}{2} = \frac{\hat{\sigma}_{\mathbf{1}} \rho' \hat{\sigma}_{\mathbf{1}} + \hat{\sigma}_{\nu} \rho' \hat{\sigma}_{\nu}}{2} = \frac{1}{2\pi} \int_0^{2\pi} d\gamma e^{-i\gamma \hat{\sigma}_{\nu}} \rho' e^{i\gamma \hat{\sigma}_{\nu}}. \quad (I5)$$

These three terms represent respectively measuring-and-forgetting, random gate application, and phase randomization. Their equivalence can be understood more formally from the standpoint of the stochastic master equation, to which Ref. [S27] provides an accessible introduction. This approach is also related to the Quantum Zeno Effect, in which persistent measurement along an axis of interest ‘‘pins’’ the qubit state to that axis by continuously dephasing any rotations away from it [S28].

Finally, we calculate the additional error introduced to the DME algorithm by the use of QME. For this, we return to the specific case where $\rho = |0\rangle\langle 0|$ (though this also generalizes to arbitrary ρ). As in Appendix H, we apply the

unitary $e^{-i\text{SWAP}\delta}$ to the joint state $\sigma \otimes |0\rangle\langle 0|$, and then randomly apply one of the unitaries $\{\hat{\sigma}_1, \hat{\sigma}_Z\}$ to the instruction qubit. Then, it can be shown that the total state of instruction and target qubit is given by

$$\begin{aligned} & \frac{1}{2} \left(e^{-i\text{SWAP}\delta} \left[\sigma \otimes |0\rangle\langle 0| \right] e^{i\text{SWAP}\delta} + (\hat{\sigma}_1 \otimes \hat{\sigma}_Z) e^{-i\text{SWAP}\delta} \left[\sigma \otimes |0\rangle\langle 0| \right] e^{i\text{SWAP}\delta} (\hat{\sigma}_1 \otimes \hat{\sigma}_Z) \right) \\ & = \underbrace{\mathcal{E}_{\delta\text{SWAP}}^{\rho=|0\rangle\langle 0|}(\sigma) \otimes |0\rangle\langle 0|}_{\text{DME}} - \underbrace{\sin^2(\delta) \langle 1|\sigma|1\rangle \left[|0\rangle\langle 0| \otimes \hat{\sigma}_Z \right]}_{\text{QME error}}, \end{aligned} \quad (\text{I6})$$

where $\mathcal{E}_{\delta\text{SWAP}}^{\rho=|0\rangle\langle 0|}(\sigma)$ is the quantum channel defined in Eq. (H9). Note that the first term, $\mathcal{E}_{\delta\text{SWAP}}^{\rho=|0\rangle\langle 0|}(\sigma) \otimes |0\rangle\langle 0|$ is exactly the desired state which can be used for the next round of DME. On the other hand, the second term $\sin^2(\delta) \langle 1|\sigma|1\rangle \left[|0\rangle\langle 0| \otimes \hat{\sigma}_Z \right]$ can be treated as an error. To find the contribution of this term in the total error, we use the fact that the trace-norm is non-increasing under any trace-preserving quantum operation \mathcal{F} : $\|\mathcal{F}(X)\|_{\text{tr}} \leq \|X\|_{\text{tr}}$, where $\|\cdot\|_{\text{tr}}$ is trace norm, *i.e.* sum of the absolute value of the eigenvalues of the operator.

For the second term in Eq. (I6) we have

$$\left\| \sin^2(\delta) \langle 1|\sigma|1\rangle \left[|0\rangle\langle 0| \otimes \hat{\sigma}_Z \right] \right\|_{\text{tr}} = 2 \sin^2(\delta) \langle 1|\sigma|1\rangle \leq 2 \sin^2(\delta). \quad (\text{I7})$$

Therefore, the additional error introduced by each application of QME is bounded by $2 \sin^2(\delta)$.

Repeating this process N times, and using the triangle inequality for the trace norm, we find that the distance between the final total system state and the state produced by DME is bounded by $2N \sin^2(\delta)$. Choosing $\delta = \theta/N$, we find that the overall additional error introduced by the use of QME is bounded by

$$2N \sin^2(\delta) = 2N \sin^2\left(\frac{\theta}{N}\right) \leq \frac{2\theta^2}{N}. \quad (\text{I8})$$

The right hand side of Eq. (I8) is the QME-induced error contribution cited in the main text.

Appendix J: Quantifying the impacts of finite QME randomizations

To properly implement the probabilistic nature of the QME operation we instantiate each DME_2 circuit a number of times. Consider as an example the $N = 3$ version of the DME_2 circuit from Figure 3,

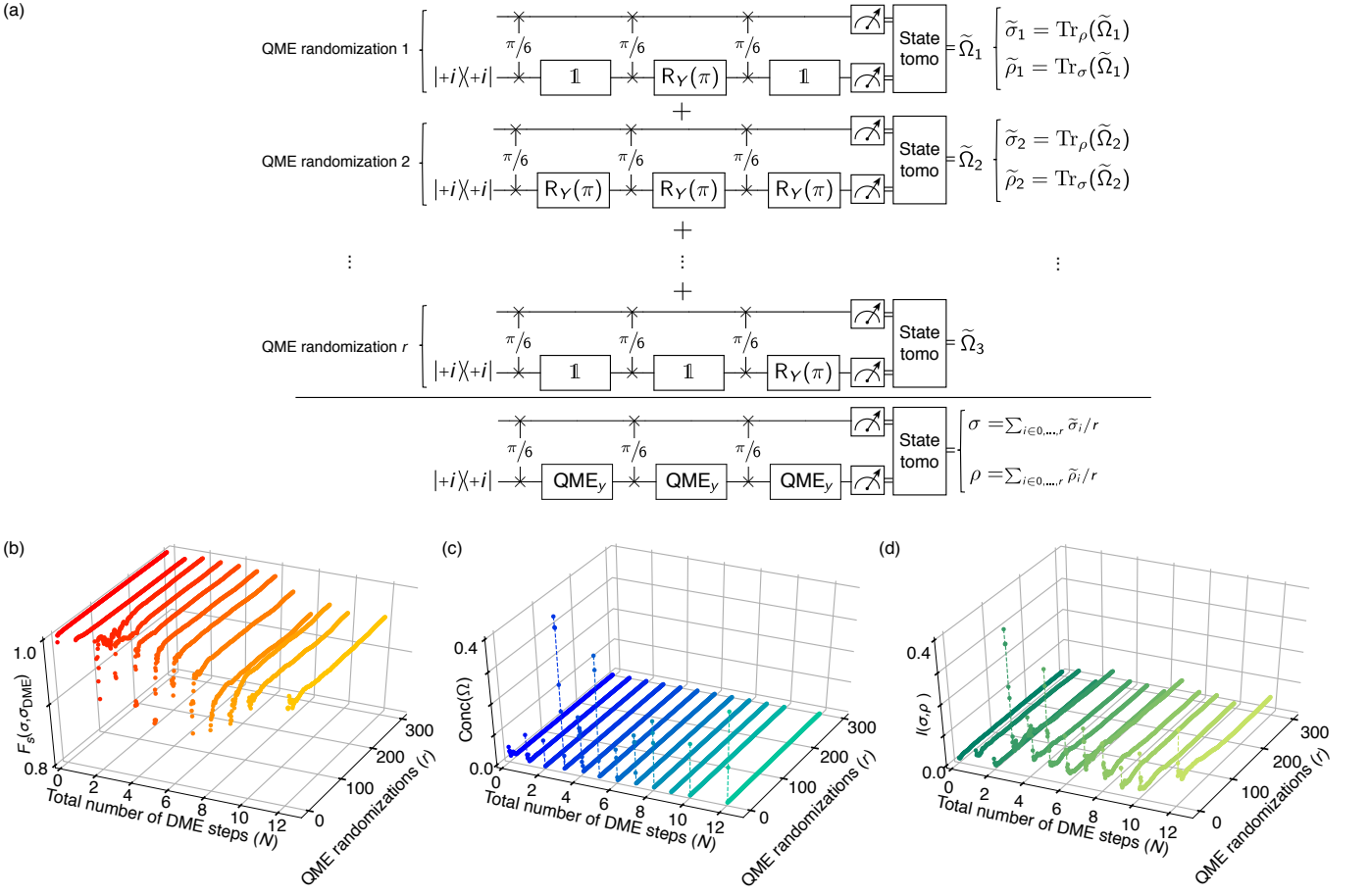
$$\sigma \text{---} \boxed{\text{DME}_2(|+i\rangle\langle +i|, 3, \pi/2)} \text{---} \sigma_{\text{out}} = \begin{array}{c} \sigma \text{---} \overset{\times}{\pi/6} \text{---} \overset{\times}{\pi/6} \text{---} \overset{\times}{\pi/6} \text{---} \sigma_{\text{out}} \\ \text{---} \underset{\times}{|+i\rangle\langle +i|} \text{---} \boxed{\text{QME}_y} \text{---} \boxed{\text{QME}_y} \text{---} \boxed{\text{QME}_y} \end{array} \quad (\text{J1})$$

In this case, each QME presents a random choice between applying $\text{R}_Y(\pi)$ or $\mathbb{1}$ at each occurrence. For an N step DME_2 there are 2^N configurations of QME gates. In the experiment it is infeasible to sample all 2^N realizations, and instead we sample a smaller number, denoted r . The circuits below show $r = 3$ random example realizations of the circuit,

$$\begin{array}{c} \overset{\times}{\pi/6} \text{---} \overset{\times}{\pi/6} \text{---} \overset{\times}{\pi/6} \text{---} \\ \text{---} \underset{\times}{\mathbb{1}} \text{---} \boxed{\text{R}_Y(\pi)} \text{---} \underset{\times}{\mathbb{1}} \end{array}, \quad \begin{array}{c} \overset{\times}{\pi/6} \text{---} \overset{\times}{\pi/6} \text{---} \overset{\times}{\pi/6} \text{---} \\ \text{---} \underset{\times}{\text{R}_Y(\pi)} \text{---} \boxed{\text{R}_Y(\pi)} \text{---} \boxed{\text{R}_Y(\pi)} \end{array}, \quad \begin{array}{c} \overset{\times}{\pi/6} \text{---} \overset{\times}{\pi/6} \text{---} \overset{\times}{\pi/6} \text{---} \\ \text{---} \underset{\times}{\mathbb{1}} \text{---} \boxed{\mathbb{1}} \text{---} \boxed{\text{R}_Y(\pi)} \end{array} \quad (\text{J2})$$

In the experiment, a total r_{QME} of circuits are executed, providing a sample from which we can extract average properties. The generic process for extracting average properties over r instantiations is sketched in Extended Data Fig. 7.

From the datasets used in the main paper, we can also explore algorithmic behavior as the randomizations of QME increase toward the central limit. In Extended Data Fig. 7b-d we plot three relevant figures of merit as a function of r and N for the $\theta = \pi$ dataset of Figure 3 in the main text. Extended Data Fig. 7b shows the evolution of the state fidelity of the output state as a function of r . For all values of N we observe that after approximately ~ 50 randomizations the effect of introducing more circuits with random choices of QME gates does not significantly alter the result. Extended Data Fig. 7c shows the concurrence of the two-qubit density matrix, a measurement of bi-partite



EXTENDED DATA FIG. S8. (a) Schematic definition of experimental execution of a DME protocol using QME operations (i.e., DME₂). (b) The state fidelity between the measured output state and the result of ideal gates implementing DME, as the number of QME randomizations are increased. (c) Concurrence in the two-qubit density matrix Ω (the combined state of the system), for increasing number of QME randomizations. (d) The mutual information between the two subsystems σ and ρ , as more randomizations of QME are used.

entanglement in the system [S29]. After just a few randomizations $r > 10$, concurrence goes to zero, indicating that (quantum) correlations have been suppressed, as expected. There may also be classical correlations between the σ and ρ subsystems. In Extended Data Fig. 7d we therefore plot the mutual information $I(\sigma, \rho)$ between each subsystem, where

$$I_{\Omega}(\sigma, \rho) = S(\text{Tr}_{\sigma}(\Omega)) + S(\text{Tr}_{\rho}(\Omega)) - S(\Omega) \quad (\text{J3})$$

is the mutual information, and $S(\Omega) = -\text{Tr}(\Omega \ln \Omega)$ is the von Neumann entropy of the density matrix Ω . Here we again observe that after $r > 10$ any correlations between the subsystems are effectively removed.

-
- [S1] Koch, J. *et al.* Charge-insensitive qubit design derived from the Cooper pair box. *Physical Review A* **76**, 042319 (2007).
[S2] Hutchings, M. D. *et al.* Tunable superconducting qubits with flux-independent coherence. *Phys. Rev. Applied* **8**, 044003 (2017).
[S3] Barends, R. *et al.* Coherent Josephson Qubit Suitable for Scalable Quantum Integrated Circuits. *Phys. Rev. Lett.* **111**, 080502 (2013).
[S4] Klimov, P. *et al.* Fluctuations of Energy-Relaxation Times in Superconducting Qubits. *Phys. Rev. Lett.* **121**, 090502 (2018).
[S5] Burnett, J. J. *et al.* Decoherence benchmarking of superconducting qubits. *npj Quantum Inf* **5**, 1–8 (2019).
[S6] Krantz, P. *et al.* A quantum engineer's guide to superconducting qubits. *App. Phys. Rev.* **6**, 021318 (2019).
[S7] Kelly, J. *et al.* Optimal Quantum Control Using Randomized Benchmarking. *Phys. Rev. Lett.* **112**, 240504 (2014).

- [S8] Strauch, F. W. *et al.* Quantum Logic Gates for Coupled Superconducting Phase Qubits. *Phys. Rev. Lett.* **91**, 167005 (2003).
- [S9] Rol, M. *et al.* Fast, High-Fidelity Conditional-Phase Gate Exploiting Leakage Interference in Weakly Anharmonic Superconducting Qubits. *Phys. Rev. Lett.* **123**, 120502 (2019).
- [S10] Martinis, J. M. & Geller, M. R. Fast adiabatic qubit gates using only sigmaz control. *Physical Review A* **90**, 022307 (2014).
- [S11] Oliver, W. D. *et al.* Mach-zehnder interferometry in a strongly driven superconducting qubit. *Science* **310**, 1653–1657 (2005). <https://science.sciencemag.org/content/310/5754/1653.full.pdf>.
- [S12] Barends, R. *et al.* Superconducting quantum circuits at the surface code threshold for fault tolerance. *Nature* **508**, 500–503 (2014).
- [S13] Chen, Z. *Metrology of Quantum Control and Measurement in Superconducting Qubits*. Ph.D. thesis, University of California, Santa Barbara (2018).
- [S14] Wallman, J., Granade, C., Harper, R. & Flammia, S. T. Estimating the coherence of noise. *New J. Phys.* **17**, 113020 (2015).
- [S15] Proctor, T., Rudinger, K., Young, K., Sarovar, M. & Blume-Kohout, R. What Randomized Benchmarking Actually Measures. *Phys. Rev. Lett.* **119**, 130502 (2017).
- [S16] Wallman, J. J. Randomized benchmarking with gate-dependent noise. *Quantum* **2**, 47 (2018).
- [S17] Vatan, F. & Williams, C. Optimal quantum circuits for general two-qubit gates. *Phys. Rev. A* **69**, 032315 (2004).
- [S18] Cirq-v0.5.0. A python library for writing, manipulating, and optimizing quantum circuits and running them against quantum computers and simulators. <https://github.com/quantumlib/cirq>.
- [S19] Nielsen, M. A. & Chuang, I. L. *Quantum Computation and Quantum Information: 10th Anniversary Edition* (Cambridge University Press, New York, NY, USA, 2011).
- [S20] McKay, D. C., Wood, C. J., Sheldon, S., Chow, J. M. & Gambetta, J. M. Efficient ZZ gates for quantum computing. *Phys. Rev. A* **96**, 22330 (2017).
- [S21] Chow, J. M. *et al.* Detecting highly entangled states with a joint qubit readout. *Physical Review A* **81** (2010).
- [S22] Banaszek, K., D’Ariano, G. M., Paris, M. G. A. & Sacchi, M. F. Maximum-likelihood estimation of the density matrix. *Phys. Rev. A* **61**, 010304 (1999).
- [S23] Knee, G. C., Bolduc, E., Leach, J. & Gauger, E. M. Quantum process tomography via completely positive and trace-preserving projection. *Phys. Rev. A* **98**, 062336 (2018).
- [S24] Efron, B. Bootstrap methods: Another look at the jackknife. *Ann. Statist.* 1–26.
- [S25] Wilde, M. M. *Quantum Information Theory 2nd ed.* (Cambridge University Press, 2017).
- [S26] Nielsen, M. A. A simple formula for the average gate fidelity of a quantum dynamical operation. *Phys. Lett. A* **303**, 249–252 (2002).
- [S27] Jacobs, K. & Steck, D. A. A straightforward introduction to continuous quantum measurement. *Contemporary Physics* **47**, 279–303 (2006).
- [S28] Itano, W. M., Heinzen, D. J., Bollinger, J. & Wineland, D. Quantum zeno effect. *Physical Review A* **41**, 2295 (1990).
- [S29] Wootters, W. K. Entanglement of Formation of an Arbitrary State of Two Qubits. *Phys. Rev. Lett.* **80**, 2245–2248 (1998).